Secondary instabilities in swept-wing boundary layers: Direct Numerical Simulations and BiGlobal stability analysis

Casacuberta Puig, J.; Groot, K.J.; Hickel, S.; Kotsonis, M.

Important note
To cite this publication, please use the final published version (if applicable).
Please check the document version above.

Secondary instabilities in swept-wing boundary layers: Direct Numerical Simulations and BiGlobal stability analysis

Jordi Casacuberta*
Delft University of Technology, Delft, The Netherlands, 2629HS

Koen J. Groot[†]
Texas A&M University, College Station, TX, USA, 77840

Stefan Hickel[‡], Marios Kotsonis[§]
Delft University of Technology, Delft, The Netherlands, 2629HS

The evolution of secondary instabilities in a three-dimensional stationary-crossflow-dominated boundary layer is investigated by means of Direct Numerical Simulations (DNS) and linear spanwise BiGlobal stability analysis. Single-frequency unsteady disturbances and a critical stationary crossflow mode are considered. Unsteady perturbation content at 1 kHz manifests in the form of the *type*-III instability mechanism in the lower portion of the boundary layer in both the DNS and the stability approach. Considering disturbances at 6 kHz, the results from the stability analysis reveal the existence of largely amplified *type*-I and *type*-II secondary instability mechanisms. Strong growth displayed by the former is measured in the DNS, which potentially overshadows manifestations of the *type*-II mechanism. Laminar-turbulent transition primarily induced by the growth of *type*-I disturbances is captured in the 6 kHz case. Overall, we report good agreement between DNS and stability analysis in terms of perturbation organization and growth rate for all cases studied.

Nomenclature

f_0	=	fundamental temporal frequency
β_0	=	fundamental spanwise wavenumber
$(\cdot)_B$	=	base flow variable
$(\cdot)_{DB}$	=	distorted base flow variable
$(\mathring{\cdot})$	=	stationary perturbation variable measured from the unperturbed base flow
$(\cdot)'$	=	unsteady perturbation variable measured from the distorted base flow
k	=	index of perturbations with temporal frequency $k f_0$
j	=	index of perturbations with spanwise wavenumber $j\beta_0$
$\lvert \cdot \rvert_{(k,j)}$	=	amplitude function of a Fourier coefficient (k, j)
δ_0	=	characteristic length
u_∞	=	characteristic velocity

*PhD Candidate, Section of Aerodynamics, Faculty of Aerospace Engineering, Correspondence: J.CasacubertaPuig@tudelft.nl.

[†]Assistant Research Scientist, Aerospace Department

[‡]Full Professor, Section of Aerodynamics, Faculty of Aerospace Engineering.

[§]Associate Professor, Section of Aerodynamics, Faculty of Aerospace Engineering.

I. Introduction

$\mathbf{A}$DVANCES in laminar-turbulent transition research in three-dimensional boundary layers have been historically motivated by the need to understand and control the transition process in swept-wing flows. Significant reduction of aircraft drag and hence fuel consumption has been shown possible by achieving laminar flow on wings, tail, and nacelles (Henke, 1999, Malik et al., 2015). Despite significant progress over the last decades, maintaining laminar flow on the wings of subsonic transport aircraft remains a major challenge. Degradation of laminar flow is generally attributed to the impact of surface irregularities such as insect contamination or steps in the juncture between wing panels. The inability of classic boundary-layer stability methods to model the effect of such surface irregularities poses a challenge for systematic transition-prediction studies. This particularly concerns the sensitivity of the unsteady mechanisms leading to laminar-turbulent transition to distortions of the primary base state due to the presence of surface roughness (Rius-Vidales and Kotsonis, 2021).

Laminar-turbulent transition in swept-wing boundary layers in smooth configurations is typically initiated by the primary crossflow instability (Mack, 1984, Saric et al., 2003). The underlying laminar base state –the so-called *unperturbed* base flow– is subject to an inflectional instability and supports the exponential growth of *small*-amplitude perturbations. The receptivity of the boundary layer to surface imperfections and free-stream disturbances mainly governs whether the primary instability manifests in the form of either travelling or stationary (zero temporal frequency) wave-like perturbations (Deyhle and Bippes, 1996, Bippes, 1999). The present work focuses on stationary-crossflow-dominated environments, which is the prevalent scenario in low-disturbance backgrounds as in free-flight (Saric et al., 2003). Under these circumstances, stationary (crossflow) vortices develop and modulate the boundary layer. The axes of the vortices are approximately aligned with the *local* trajectory of the streamlines in the inviscid region far from the wall.

Laminar breakdown in a stationary-crossflow-dominated boundary layer is typically preceded by a stage of non-linear growth and saturation of the stationary crossflow perturbation. As such, traditional transition-prediction methods that rely on linear stability theory (Mack, 1984, Reed et al., 1996, Theofilis, 2003), as for instance the e^N method (Van Ingen, 1956, Smith and Gamberoni, 1956), are unsuitable for predicting the onset of transition. Early experiments showed that measured perturbation growth rates differ from those predicted by linear stability analysis when sufficiently large perturbation amplitudes are attained (Müller, 1990, Kachanov and Tararykin, 1990, Bippes, 1991). The Non-linear Parabolized Stability Equations (NPSE) technique was later proven capable of modeling the stages of strong non-linear crossflow-perturbation evolution; see Bertolotti (1996), for instance. Stability analyses carried out with NPSE further confirmed that major discrepancies between experiments and theoretical results were caused by the non-linear saturation of the crossflow vortices (Haynes and Reed, 2000).

The *distorted* base flow, i.e., the base state non-linearly deformed by the primary crossflow mechanism, is prone to secondary instability amplification. Due to the broad range of flow states and *perturbation*-quantity definitions in the crossflow problem, the following nomenclature is introduced: letting $\boldsymbol{q}$ be the vector of state variables $\boldsymbol{q} = [\boldsymbol{v} \; p]^{\mathrm{T}} = [u \; v \; w \; p]^{\mathrm{T}}$, the instantaneous flow field is decomposed as

$$\boldsymbol{q}(x, y, z, t) = \underbrace{\boldsymbol{q}_{\mathrm{B}}(x, y) + \mathring{\boldsymbol{q}}(x, y, z)}_{\boldsymbol{q}_{\mathrm{DB}}} + \boldsymbol{q}'(x, y, z, t), \tag{1}$$

where u, v, w denote the chordwise, wall-normal, and spanwise velocity components, respectively, and p is the static pressure. The field $\boldsymbol{q}_{\mathrm{B}}$ is the unperturbed laminar base flow, which under the infinite-span assumption is conceived as a spanwise-invariant solution. The field $\mathring{\boldsymbol{q}}$ is the stationary crossflow perturbation and $\boldsymbol{q}_{\mathrm{B}} + \mathring{\boldsymbol{q}}$ forms the distorted base flow, $\boldsymbol{q}_{\mathrm{DB}}$. Lastly, $\boldsymbol{q}'$ denotes the unsteady perturbations developing with respect to $\boldsymbol{q}_{\mathrm{DB}}$.

In the distorted base flow, the co-rotating crossflow vortices redistribute momentum by displacing low-momentum fluid upward and high-momentum fluid towards the wall. Strong shear layers develop as a consequence of such momentum redistribution. The distorted inflectional velocity profiles support the growth of unsteady secondary instabilities, ultimately responsible for laminar breakdown. Secondary perturbations displaying a high-frequency content were initially identified in swept-cylinder (Poll, 1985), swept-wing (Deyhle and Bippes, 1996, Kohama et al., 1991), and swept-Hiemenz (Malik et al., 1994) flow configurations. Considering a swept-wing boundary layer, Malik et al. (1999) report two families of secondary instability eigenmodes using Secondary Linear Stability Theory (SLST). The *type*-I (or z-)mode is produced most strongly by the spanwise shear in the outer part of the upwelling region of the primary crossflow vortex (or: "on its shoulder"). The *type*-II (or y-)mode, on the other hand, gains its energy primarily from the wall-normal shear and is located on top of the crossflow vortex. Theoretical results of Fischer and Dallmann (1991) identify a low-frequency eigenmode dominant in the near-wall shear layer of the crossflow vortex, which is nowadays referred to as *type*-III (Koch et al., 2000). It is commonly interpreted as the primary traveling crossflow mechanism

distorted by the action of the stationary crossflow mechanism.

Direct Numerical Simulations (DNS) of Högberg and Henningson (1998) of a Falkner-Skan-Cooke boundary layer reveal *type*-I and *type*-III structures; however, manifestations of the *type*-II eigenmode are not observed. Högberg and Henningson (1998) postulate that, in a low-disturbance environment, laminar transition is triggered by high-frequency instabilities, inasmuch as they display larger growth rates than the low-frequency ones. Contrarily, in high-disturbance conditions, low-frequency instabilities may dominate the transition process since their onset is placed at a more upstream location than the high-frequency ones (Högberg and Henningson, 1998). In line with findings of Högberg and Henningson (1998), Wassermann and Kloker (2002) identify in their DNS the high-frequency *type*-I and low-frequency *type*-III instability mechanisms. *Type*-II perturbations are argued to arise only in *less physically relevant* cases, as for instance, when the primary crossflow vortex has a subcritical spanwise wavelength. In such cases, the narrow spacing between the stationary vortices potentially weakens the *type*-I amplification, which may facilitate the development of *type*-II disturbances (Wassermann and Kloker, 2002). Nonetheless, in the recent years, manifestations of the *type*-II mechanism in numerical simulations have been widely reported (Li et al., 2016, 2017). The *type*-I,-II,-III mechanisms have been identified experimentally as well; see for instance Serpieri and Kotsonis (2016) for a detailed characterization of the secondary instabilities using Particle Image Velocimetry (PIV).

Even though a broad body of knowledge on secondary instabilities has been developed during the last two decades, to establish a criterion for breakdown onset from a single major base-flow property remains a challenge (Wassermann and Kloker, 2002). More elaborate techniques consider secondary *N*-factor correlation methods, as suggested by Malik et al. (1999). Nevertheless, the existence of multiple unstable secondary eigensolutions poses a challenge for systematic transition-prediction methodologies (Li et al., 2017). Although secondary stability analyses are reasonably efficient methods for perturbation growth rate computations, the literature reports disagreement between DNS and SLST with regard to the role played by the *type*-II mechanism. The SLST generally predicts large growth rates for this instability mechanism (Malik et al., 1999, Koch et al., 2000), which does not correspond to the observed behaviour in DNS (Högberg and Henningson, 1998, Wassermann and Kloker, 2002, Bonfigli and Kloker, 2007).

White and Saric (2005) ascribe the aforementioned discrepancies to receptivity mechanisms. Bonfigli and Kloker (2007), on the other hand, attribute inconsistencies in the literature to inaccuracies of the growth rates from SLST. Moreover, the results provided by SLST are found to be very sensitive to the representation of the distorted base flow in the stability problem. Groot et al. (2018) have applied BiGlobal stability analysis to experimentally measured base flows and deepened into the stability characteristics of the *type*-I and *type*-II mechanisms. In our present work, the novelty with respect to the work of Groot et al. (2018) lies in that the two-dimensional stability problem is solved using a non-orthogonal coordinate system, similar to the approach presented by Li and Choudhari (2011). Accordingly, the conditions of periodicity in the spanwise direction and flow quasi-invariance in the direction of the crossflow-vortex axis can be accounted for simultaneously. The use of a non-orthogonal coordinate system moreover enables solving an important issue brought up in the literature. As one of the shortcomings of computing the distorted basic state necessary for the stability approach with DNS, Bonfigli and Kloker (2007) describe (see their § 4.2) that "the basic assumptions of the [stability analysis] are not sufficient to determine the extraction procedure [of the distorted base flow] uniquely". Hence, they defined 3 alternative extraction procedures, which ensured the satisfaction of the continuity equation for the distorted base flow in 3 different *orthogonal* coordinate systems, while adhering to the slow-evolution hypotheses underlying the stability analysis. By the advent of the approach of Li and Choudhari (2011), incorporating non-orthogonal coordinates, this ambiguity is uniquely resolved: data are extracted in planes in which the flow field satisfies the continuity equation as formulated in the DNS, while the (non-orthogonal) out-of-plane direction is aligned with the direction of least variation of the distorted base flow.

The discrepancies reported in the literature with regard to secondary instability behaviour prediction between DNS and stability analysis have motivated the present work. In this article, we study the *type*-I and *type*-III instability evolution in a stationary-crossflow-dominated boundary layer developing over a flat plate. DNS of the stationary distorted base flow is performed. Secondary instability mechanisms are then triggered via upstream forcing of selected (monochromatic) temporal frequencies corresponding to 1 kHz and 6 kHz. In addition, we carry out a linear spanwise BiGlobal stability analysis on the distorted DNS base flow. A full comparison between disturbance growth-rate evolution and topology between both methods is provided. The article is structured as follows: Section II introduces the flow problem and the setup of the DNS. Section III describes the topology of the distorted base flow and the formulation of the BiGlobal stability problem. Section IV analyzes the unsteady disturbance behaviour and compares the results from DNS and BiGlobal analysis. Finally, Section V presents the conclusions of this work.
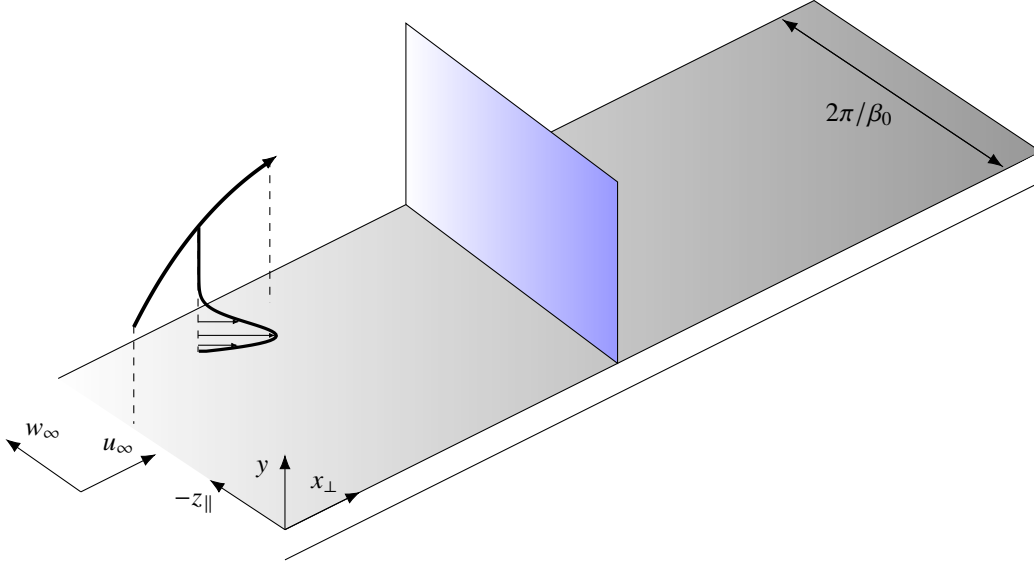
Figure 1   Sketch of the flow problem: flat plate, external inviscid streamline with associated crossflow profile, flat-plate-aligned coordinate system $(x_\perp, y, z_\parallel)$, **and BiGlobal plane.**

II. Setup of the DNS

Two methods are considered in this work to compute secondary-crossflow-instability evolution: Direct Numerical Simulations (DNS) and spanwise BiGlobal stability analysis applied on the distorted base flow provided by DNS. The present section first introduces the geometry and flow problem and describes the setup of the DNS.

A. Steady DNS

Upon replicating the setup of Rius-Vidales and Kotsonis (2021), the swept-wing flow problem is modeled as flat-plate flow with an imposed external airfoil-like pressure gradient. Data obtained from independent experiments carried out at TU Delft on a 45° swept wing (Rius-Vidales and Kotsonis, 2021) are employed to model the acceleration of the freestream in the chordwise direction, $x_\perp$. The stationary distorted base flow q_{DB} is obtained by performing DNS of the three-dimensional incompressible Navier-Stokes equations. The numerical computations are carried out in a sequential manner; first, we compute the spanwise-invariant unperturbed base flow, q_B. This base-flow solution then serves as initial condition for the computation of the steady-state $q_{DB} = q_B + \mathring{q}$, with $\mathring{q}$ denoting the stationary-crossflow-perturbation field (Eq. 1).

The computational domain is swept and aligned with the spanwise direction of the wing, $z_\parallel$. The coordinate y denotes the wall-normal direction. The instantaneous velocity vector $\boldsymbol{v} = [u\ v\ w]^T$ expresses the velocity components aligned with the flat-plate-based orthogonal coordinate system. The flow problem is illustrated in Fig. 1. The inflow, which here corresponds to $x_\perp = 0$, is virtually placed at 5% of the chord of the wing model used in the experiments. The effect of the sweep angle is accounted for by decomposing the inflow free-stream velocity into components parallel, u_∞, and perpendicular, w_∞, to $x_\perp$. In the present configuration, $w_\infty/u_\infty = -1.24$. The inflow boundary layer thickness, $\delta_0 = 7.71 \times 10^{-4}$ m, and the inflow free-stream velocity, $u_\infty = 15.10$ m/s, are the characteristic quantities used to non-dimensionalize the flow problem.

The DNS are carried out with INCA, a conservative finite-volume-based flow solver (Hickel and Adams, 2008, Hickel et al., 2014, Casacuberta et al., 2020). The free-stream evolution and the DNS setup considered in this work are identical to the ones presented in a recent article (Casacuberta et al., 2021). The highly refined computational grid for the current DNS computations has 6760, 576, and 72 points along the chordwise, wall-normal, and spanwise directions, respectively, and more than 70 grid points cover the inflow boundary-layer thickness. Considering the unperturbed base-flow solution, the minimum grid spacing in wall units is $\Delta x_\perp^+ = 5.68$, $\Delta y^+ = 0.52$, $\Delta z_\parallel^+ = 4.73$. A high level of refinement is maintained in the upper portion of the crossflow vortex. In Fig. 3 we show matching perturbation amplitudes between the results of DNS and an independent non-linear stability analysis performed on the

4

DNS unperturbed base flow using the NPSE method (Westerbeek, 2020).

To trigger stationary crossflow growth, the laminar inflow is perturbed with a stationary crossflow mode pre-calculated using Linear Stability Theory. While being left free to grow in $x_\perp$, the crossflow disturbance is constrained to be periodic in $z_\parallel$ by imposing periodic boundary conditions at the transverse boundaries; the spanwise domain length, $\lambda_z = 2\pi/\beta_0 = 7.5$ mm, is set equal to the spanwise wavelength of the fundamental crossflow instability. The main stability features of the stationary-crossflow field are recovered from the DNS by spanwise-Fourier decomposition of the perturbation-velocity field:

$$\hat{\boldsymbol{v}}(x_\perp, y, z_\parallel) = \sum_{j=-N}^{j=N} \hat{\boldsymbol{v}}_{(0,j)}(x_\perp, y) \, e^{ij\beta_0 z_\parallel}, \tag{2}$$

where $\hat{\boldsymbol{v}}_{(0,j)} \in \mathbb{C}$ denotes the coefficients of the Fourier expansion, N is the number of modes considered, and $i^2 = -1$. The nomenclature $(0, j)$ denotes the jth stationary (zero temporal frequency) perturbation Fourier mode. Furthermore, hereafter we refer to the modulus of the components of $\hat{\boldsymbol{v}}_{(0,j)}$ as amplitude functions. The amplitude function associated to the chordwise-velocity perturbation component, $|\hat{u}|_{(0,j)}$, is used to characterize stationary crossflow evolution. In particular, $|\hat{u}|_{(0,j)}$ measured at the wall-normal location of its peak value, $\hat{A}^u_{(0,j)}(x)$, is the main metric used to quantify stationary crossflow growth in $x_\perp$.

B. Unsteady DNS

The secondary perturbation evolution in the DNS is numerically triggered by applying unsteady forcing. A disturbance strip placed sufficiently upstream *locally* modulates the wall-normal velocity at the wall ($y = 0$) as follows:

$$v(x_\perp, 0, z_\parallel, t) = A_0 \, f_f(x_\perp) \cos(\beta_0 z_\parallel + \omega_0 t), \tag{3}$$

where $\omega_0 = 2\pi f_0$ and $A_{0(k,j)}$ are the fundamental angular frequency and amplitude of the wall disturbances, respectively, and

$$f_f(x_\perp) = \left(\frac{4 \left(x_\perp - x_{\perp,\text{start}} \right) \left(x_{\perp,\text{end}} - x_\perp \right)}{(x_{\perp,\text{end}} - x_{\perp,\text{start}})^2} \right)^3, \tag{4}$$

is a smooth function which modulates the wall-normal velocity in $x_\perp$. The functional f_f has vanishing first and second derivatives at $x_{\perp,\text{start}}$ and $x_{\perp,\text{end}}$, the starting and ending positions of the disturbance strip, respectively. It is noted that this unsteady forcing method does not add a net mass into the domain. Wassermann and Kloker (2002) consider a similar approach to numerically investigate crossflow instabilities. In the outflow region, a damping zone is used to reduce unsteady fluctuations and avoid possible reflections. The damping zone, which starts at $x_\perp/\delta_0 = 475$, relies on a temporal-filter technique through the application of the Selective Frequency Damping (SFD) method (Akervik et al., 2006, Casacuberta et al., 2018).

In this work, monochromatic (i.e., single temporal frequency) unsteady forcing is applied. DNS for two different fundamental frequencies, $f_0 = 1$ kHz and 6 kHz, are performed and analyzed independently. A BiGlobal stability analysis performed *a priori* revealed that the aforementioned values are expected to yield manifestations of the *type*-I, -II, and -III mechanisms. The wall forcing is placed closely upstream of the neutral point for each considered frequency, as indicated by the stability analysis. In particular, we choose to place the start of the disturbance strip, $x_{\perp,\text{start}}$, $24\delta_0$ upstream of the corresponding neutral point; this length represents approximately two times the *local* streamwise wavelength of the primary stationary-crossflow component. Accordingly, $x_{\perp,\text{start}}/\delta_0 = 201, 251$, for $f_0 = 1$ kHz and 6 kHz, respectively and $x_{\perp,\text{end}} - x_{\perp,\text{start}} = 12\delta_0$ for all cases. The initial forcing amplitude in the disturbance strips, A_0 (Eq. 3), is chosen such that secondary-perturbation exponential growth is captured for a sufficiently large $x_\perp$-range downstream of the forcing location. Based on tests performed *a priori*, we choose $A_0/u_\infty = 10^{-5}$ for $f_0 = 1$ kHz and $A_0/u_\infty = 10^{-3}$ for $f_0 = 6$ kHz.

The secondary instability behaviour is analyzed from the unsteady DNS data once the disturbance strip is activated and transient flow structures are washed out. Snapshot data are collected at a rate of approximately 20 samples per period of the fundamental frequency. The perturbation-velocity field $\boldsymbol{v}'$ (Eq. 1) is Fourier decomposed in the spanwise direction and in time and expressed as a sum of modes, i.e.,

$$\boldsymbol{v}'(x_\perp, y, z_\parallel, t) = \sum_{k=-M_t}^{M_t} \sum_{j=-M_z}^{M_z} \tilde{\boldsymbol{v}}_{(k,j)}(x_\perp, y) \, e^{i\left(j\beta_0 z_\parallel - k\omega_0 t \right)}, \tag{5}$$

5
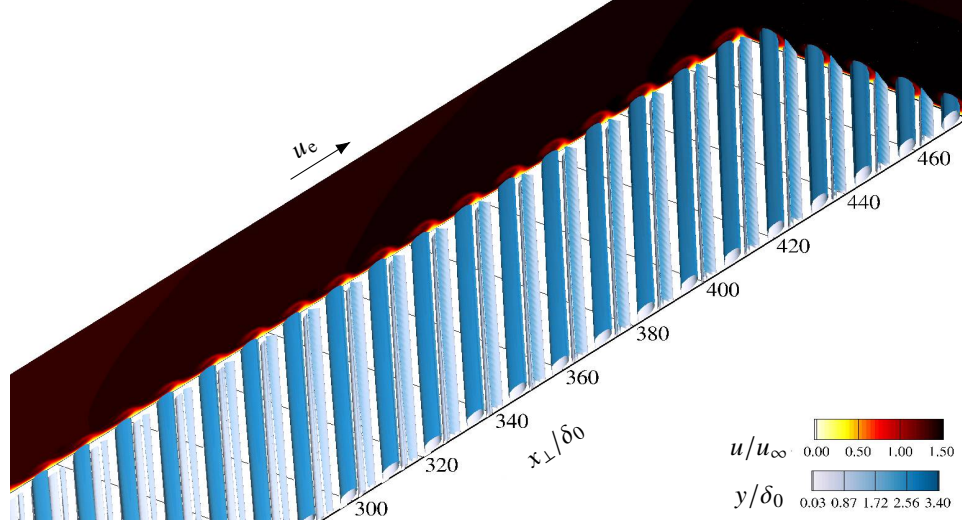
Figure 2 **Instantaneous Q-criterion isosurface colored by wall distance and y-$z_{||}$, $x_\perp$-y planes of instantaneous chordwise velocity. The DNS data are duplicated 4 times in $z_{||}$ in a periodic manner for illustration purposes.**

where $\tilde{\mathbf{v}}_{(k,j)} \in \mathbb{C}$ expresses the Fourier coefficient, and M_t, M_z indicate the number of modes. We choose $M_z = 5$. The modulus of the components of $\tilde{\mathbf{v}}_{(k,j)}$ read $|\tilde{u}|_{(k,j)}, |\tilde{v}|_{(k,j)}, |\tilde{w}|_{(k,j)}$ and are hereafter referred to as *amplitude functions*. The subscript (k, j) denotes perturbation quantities of temporal frequency $k\omega_0$ and spanwise wavenumber $j\beta_0$. The maximum along y of a corresponding amplitude function, hereafter denoted by $A^q_{(k,j)}$, where $q = u, v, w$, characterizes the perturbation *amplitude*. A corresponding perturbation growth rate is evaluated as

$$\alpha^q_{i,(k,j)} = -\frac{1}{A^q_{(k,j)}} \frac{dA^q_{(k,j)}}{dx_\perp}. \tag{6}$$

III. Formulation of the BiGlobal stability problem and distorted base-flow topology

In this section, an overview of the distorted-base-flow behaviour is presented and we introduce the formulation and the setup of the stability approach.

A. Topology of the distorted base flow

The distorted base flow features prominent co-rotating vortices whose axes of rotation are practically aligned with the *local* direction of the inviscid streamlines. Figure 2 portrays these stationary crossflow vortices in the present DNS, characterized as isosurfaces of Q-criterion (Hunt et al., 1988). The vortices grow in $x_\perp$ and induce a wavy pattern, i.e., they modulate the velocity field in the chordwise and the spanwise directions and introduce strong shear layers.

The amplification of the crossflow vortices and the associated stationary-crossflow-perturbation is illustrated in Fig. 3 portraying the chordwise evolution of the perturbation amplitude, $\hat{A}^u_{(0,j)}$, $j = 0$-5. The fundamental crossflow mode (i.e., $\mathring{\mathbf{q}}_{(0,1)}$) imposed at the inflow initially undergoes a stage of exponential amplification. The harmonic perturbation components arise gradually as they are triggered by non-linear perturbation mechanisms. To further assess the nature of the stationary perturbation mechanisms, we solve the linear and non-linear Parabolized Stability Equations (PSE) approaches on the unperturbed DNS base flow. The solution to linear PSE matches the amplitude evolution of the fundamental mode obtained from DNS up to approximately $x_\perp/\delta_0 = 180$. At this chordwise location, non-linear perturbation mechanisms start to significantly influence the evolution of $\hat{A}^u_{(0,1)}$ in the DNS. The latter is further confirmed by the agreement between the results of DNS and non-linear PSE (NPSE) further downstream (Fig. 3). After the stages of linear and non-linear growth, the perturbation system reaches saturation. The fundamental crossflow mode attains a saturation amplitude corresponding to 33% of u_e, the *local* free-stream velocity. The amplitude curves of the high-order
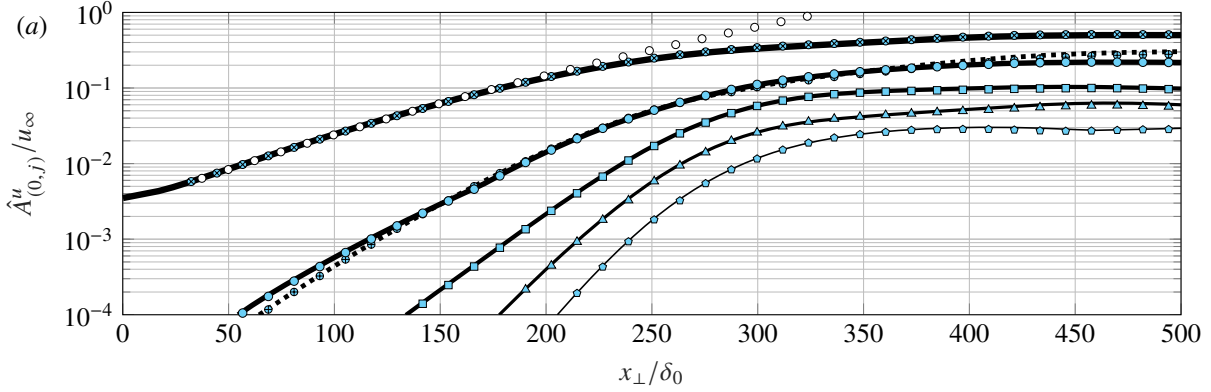
6

Figure 3 **Chordwise evolution of the stationary crossflow perturbation from DNS (lines), linear PSE (white symbols), and non-linear PSE (blue symbols). Dotted line indicates $\hat{A}^u_{(0,0)}$, solid lines express $\hat{A}^u_{(0,j)}$, $j = 1$ - 5 (thick to thin).**

harmonics reach a plateau as well, whereas the mean-flow distortion, $A^u_{(0,0)}$, maintains a positive growth rate near the outflow.

The distorted base flow is the reference primary state used in the stability problem to model the unsteady perturbation behaviour. There are two key aspects of the present distorted base flow that allow simplifying the three-dimensional linear perturbation problem. The first aspect is that the distorted base-flow field is periodic in the direction parallel to the leading edge, enabling the use of periodic boundary conditions. The second aspect is that the flow develops slowly in the direction of the axis of the crossflow vortex; while the vortex imposes a large distortion on the steady flow field, the vortex itself develops slowly downstream.

In simultaneously demanding periodicity in the spanwise direction and slow evolution along the vortical axis, it is necessary to formulate the stability problem in a system of non-orthogonal coordinates. The essentials of the formulation are presented in § VI.A. Hereafter, the x coordinate denotes the non-orthogonal "out-of-plane direction" whereas, as stated above, $x_\perp$ indicates the leading-edge-orthogonal direction (Fig. 1). The variable θ is used to indicate the angle between x and $x_\perp$, such that $\theta = 0°$ corresponds to considering the chordwise direction identically. Due to considering a negative sweep angle, $\theta < 0°$ corresponds to x pointing towards the outboard direction, i.e., in the negative $z_\parallel$ direction. The first step to formulate the stability problem is to extract the orientation of the vortical axis from the distorted base-flow variables. To be more precise, the direction is sought in which the base-flow quantities vary the least, so that dropping their derivative in that direction from the stability equations imposes the smallest modeling error.

Figure 4 depicts different representations of the derivative in question for different choices of θ. These angles are determined at a given $x_\perp$-location by: 1) computing the x-derivative along a given angle for the entire $z_\parallel$-y plane, 2) evaluating the maximum and Root-Mean-Square (RMS) of the derivative in the $z_\parallel$-y plane, and 3) varying the given angle until the minimum is found. After the crossflow vortex attains a significant magnitude, the minimum angles for the different velocity components and measures collapse onto an angle that is about 2 to 4 degrees less (in magnitude) than that corresponding to the inviscid streamline. That is, the direction corresponding to the least variation in the base flow is removed from the leading-edge-orthogonal direction by a slightly smaller extent than the inviscid streamline. This is expected as a consequence of the action of the crossflow velocity component on the crossflow vortices.

The difference in magnitude in the out-of-plane derivative is illustrated in Fig. 5. If the out-of-plane direction is not chosen appropriately, the magnitude of the derivatives becomes comparable to the strong wall-normal shear as the crossflow vortex saturates.

B. Setup of the BiGlobal stability problem

As elaborated before, the stability problem is formulated in a non-orthogonal coordinate system to minimize the model error. In particular, the unsteady linear perturbation is cast into the following form:

$$\boldsymbol{q}'(x, y, z, t) = \check{\boldsymbol{q}}(z, y)\, e^{i(\check{\alpha}x - \omega_0 t)} + \text{c.c.,} \tag{7}$$
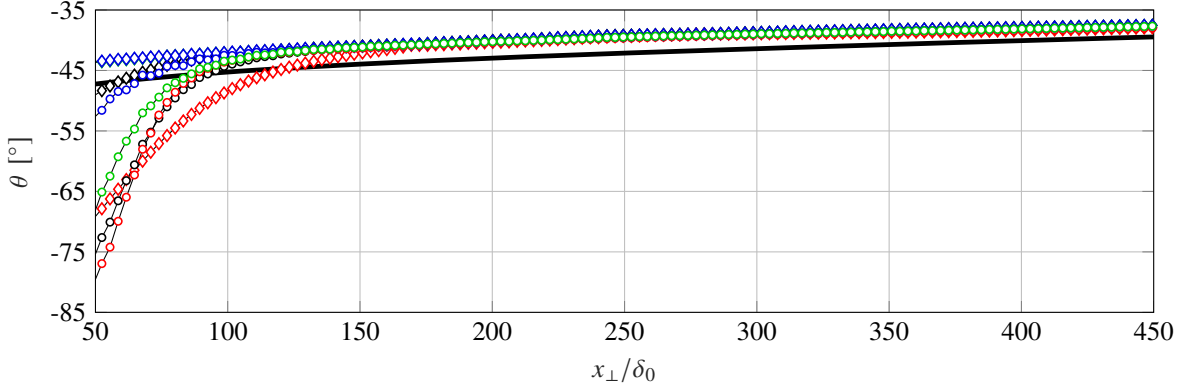
7

Figure 4   Angles indicating the direction along which the out-of-plane derivative is minimal per $x_\perp$-location:
$\partial u_{\mathbf{DB}}/\partial x$ **(black symbols),** $\partial v_{\mathbf{DB}}/\partial x$ **(red symbols),** $\partial w_{\mathbf{DB}}/\partial x$ **(blue symbols), sum of components (green symbols), maximum over** $z_\parallel y$**-plane (diamonds), rms over** $z_\parallel y$**-plane (circles), reference inviscid streamline (solid black).**

where $\check{\alpha}$ is the complex wavenumber in the non-orthogonal x-direction and $\check{\boldsymbol{q}} = [\check{u}\ \check{v}\ \check{w}\ \check{p}]^{\mathrm{T}}$ represents the corresponding two-dimensional eigenvector. The x-coordinate locally points along the vortical axis of the crossflow vortex. Note that although z is parallel to $z_{||}$, z differs from $z_{||}$ by an $x_\perp$-dependent shift; see § VI.A. The BiGlobal stability equations are obtained by substituting ansatz (7) into the linearized Navier-Stokes equations and neglecting the x-derivatives of the base-flow quantities. The resulting system of equations is given in Appendix A of Groot and Eppink (2021).

Due to the assumption that the eigenfunctions are locally independent of x, the domain can be shifted such that the z-coordinate covers the same values in the $z_{||}$-coordinate at a given x-station. Upon imposing periodic conditions for all variables in z, these conditions are imposed at the same location as where they are imposed in the DNS. The no-slip and the no-penetration conditions are applied for the perturbation velocity components and the y-momentum equation is used as a compatibility condition for the pressure at $y = 0$. At the top boundary, whose location matches the top boundary of the DNS domain, homogeneous Dirichlet conditions are used for all perturbation variables. In what follows, the spatial stability framework will be adopted, which implies that a real frequency is imposed and the BiGlobal stability equations are solved for $\check{\alpha}$, which will be complex, in general. In fact, if $\check{\alpha}_i < 0$, the perturbation grows exponentially in the x-direction.

The stability problem is discretized with a sixth-order finite-difference approach in the y- and $z_{||}$-directions in combination with the BiQuadratic mapping described in Groot et al. (2018). This approach allows prescribing a high resolution in the wall-normal direction across the very broad range considered in the streamwise direction. In the spanwise direction, the collocation nodes are mapped onto the physical domain by starting from a cosine distribution and using $(z_{||,i1}, z_{||,i2}, z_{||,\max}) = (1/3, 2/3, 1)\lambda_z$. While the cosine distribution provides a clustering toward the boundaries in order to prevent the Runge phenomenon, this setup of the BiQuadratic mapping ensures a practically-uniform node-distribution in the middle-third of the domain. In the wall-normal direction, again a cosine distribution is mapped with the parameters: $(y_{i1}, y_{i2}, y_{\max}) = (2.5, 5, 25.8)\delta_0$. Using 100 and 200 nodes in the spanwise and wall-normal directions, respectively, and $\Delta x_\perp/\delta_0 \approx 1$ results in 10^{-4} relative differences in the N-factors for all instability mechanisms at the end of the integration in the chordwise direction.

The stability results were obtained by first using the Arnoldi algorithm with an appropriate eigenvalue guess and thereafter continuing the solutions in the x-ω_0 parameter space by the use of 1) the Arnoldi, 2) a Newton-Raphson, or 3) a Rayleigh-quotient algorithm; see Pinna (2012, Appendix C) for the conceptual elaboration of the latter two approaches. Unless an eigensolution "is lost", all 3 algorithms yield matching solutions up to the set iterative tolerance for the relative error in the eigenvalue of 10^{-13}. The different algorithms were implemented in preparation of the deployment of more advanced stability approaches. It is generally observed that a solution can be lost when using the Arnoldi method as the continuation approach if the change in the eigenvalue is large and when other eigenvalues are close to the solution of interest. The Newton-Raphson and Rayleigh-quotient approaches are much more robust in this regard. The Newton-Raphson algorithm usually requires less iterations to converge, while the Rayleigh-quotient approach is observed to be more robust when deployed in regions where the change in the eigenvalue is relatively large.

In order to provide an in-depth comparison with the DNS perturbation data, the BiGlobal eigenfunctions are Fourier
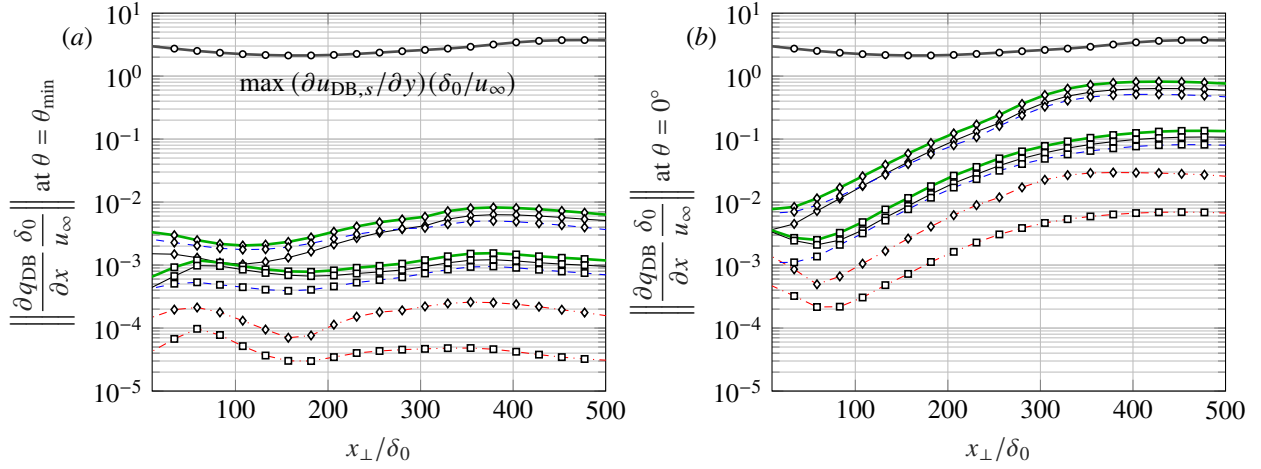
8

Figure 5   **Measures of the out-of-plane derivative in the direction of least variation (*a*) and in the chordwise direction (*b*): $\partial u_{\text{DB}}/\partial x$ (thin black), $\partial v_{\text{DB}}/\partial x$ (dash-dotted red), $\partial w_{\text{DB}}/\partial x$ (dashed blue), sum of components (thick green), maximum over $z_{\parallel}$-y plane (diamonds), rms over $z_{\parallel}$-y plane (squares). The maximum magnitude of the wall-normal derivative (thick solid gray and circles) is given for reference.**

transformed in the spanwise direction according to the following decomposition:

$$\breve{q}(z, y) = \sum_{j=-M_z}^{M_z} \breve{\breve{q}}_{(k=1,j)}(y)\, e^{i(j\beta_0 z)}, \tag{8}$$

as evaluated at a particular $x_{\perp}$-station. The numerical evaluation of Transform (8) is performed identically as the z-transform represented by Decomposition (5). Note that $\breve{q}$ is necessarily defined in the non-orthogonal z-coordinate; the data is shifted to the $z_{\parallel}$-coordinate in order to compare against the DNS data. The subscript of $\breve{\breve{q}}$ is defined analogously to the subscript of $\tilde{v}$ in Decomposition (5). Note that k is set equal to 1, inasmuch as the BiGlobal approach represents perturbations as a monochromatic signal following on ansatz (7).

9

IV. Unsteady perturbation evolution

The evolution of the unsteady disturbance field for each fundamental frequency, $f_0 = 1$ kHz and 6 kHz, is analysed in this section. Emphasis is placed on the comparison between the results from the DNS and the BiGlobal computations.

A. Overview of stability results

To provide an overview of the amplification results, they are presented in the form of N-factors defined as follows:

$$N = -\int_{x_{\text{neut}}}^{x} \check{\alpha}_i(\bar{x}) \, \mathrm{d}\bar{x} = -\int_{x_{\perp,\text{neut}}}^{x_{\perp}} \check{\alpha}_i(\bar{x}_{\perp}) \sec \theta(\bar{x}_{\perp}) \, \mathrm{d}\bar{x}_{\perp} \qquad (9)$$

where $\check{\alpha}_i$ represents the imaginary part of $\check{\alpha}$ as introduced in Eq. 7, the overbarred $\bar{x}$ and $\bar{x}_{\perp}$ represent (dummy) integration variable equivalents of x and $x_{\perp}$, and the subscript neut indicates the (most upstream) neutral point, where $\check{\alpha}_i = 0$. Only the eigenvalue is accounted for in the amplification factor, due to the local nature of the stability problem in the streamwise direction.

The overview is presented in Fig. 6, showing the streamwise evolution of the N-factors per frequency in panel (a) and the maximum N-factor in the $x_{\perp}$-direction versus the frequency in panel (b). Before interpreting Fig. 6, two aspects should be highlighted. First, all but the *type*-III N-factor curves for $f_0 \in (900; 1100)$ Hz are truncated downstream of the station $x_{\perp}/\delta_0 = 380$. Upon tracing the solution at $f_0 = 1$ kHz downstream of this point, the *type*-III eigenfunctions (dominant in the inner side of the upwelling region of the vortex) develop an (at first spatially disconnected) structure reminiscent of the *type*-II mechanism (i.e., that is located on top of the crossflow vortex) and closely resembles the structure shown in Fig. 8(a) of Groot et al. (2018) and Fig. 35 of Bonfigli and Kloker (2007). This could hence be referred to as a *type*-II/III hybrid structure. In the literature (Choudhari et al., 2013a, Li et al., 2014), a similar hybrid of the *type*-I and -II mechanisms has been previously described. Although this behavior is recovered with all 3 solvers (viz. the Arnoldi, Newton-Raphson, and Rayleigh-quotient approaches) at $f_0 = 1$ kHz, the emergence of the *type*-II structure was found to display a sensitive dependence on f_0, which resulted in an unusual distribution of the N-factor curves. This behavior is hence deemed to require a careful, further investigation, i.e. to eliminate unexpected uncertainty that could potentially be attributed to the spatial resolution, the frequency spacing, and/or the used solver. Due to the truncation of the *type*-III results in $x_{\perp}$, some lower-frequency *type*-III disturbances might attain larger amplification factors than the data in this paper presently report. Second, also the *type*-I mechanism displays a sensitive behavior for low frequencies: $f_0 < 2.8$ kHz. In this case, the eigenvalues $\check{\alpha}$ undergo a steep dive when following the solution upstream toward the (most upstream) neutral point. The solutions for $f_0 = 1.2, 1.4,$ and 1.6 kHz were carefully traced upstream, so that N-factor curves could be drawn at these frequencies. As a consequence, no calculated data (i.e. no markers) are present in-between $f_0 = 1.6$ and 2.8 kHz in Fig. 6(b). Nevertheless, the straight-line connection of the neighboring datapoints is deemed to provide a reasonable approximation of the expected results. Despite these two gaps in the parameter space, solid conclusions can be drawn from Fig. 6 in its present state.

Mostly importantly, it is observed that the *type*-I disturbance is amplified most ($N = 16.79$; at $f_0 = 5.8$ kHz; and $x_{\perp}/\delta_0 = 500$), *type*-II second-most (8.98; 8.0 kHz; 500), and *type*-III the least (4.05; 0.8 kHz; 380). In order to attempt forcing the different modes in the DNS in an isolated manner, the frequencies: 6 and 1 kHz were selected for the *type*-I and -III mechanisms, respectively. The most upstream neutral points corresponding to these mechanisms at these frequencies are located at $x_{\perp}/\delta_0 = 279$ and 225. For *type*-I, the selected frequency is close to the most amplified one. Although the *type*-III mechanism is most amplified at much lower frequencies, the *type*-I mechanism still competes in terms of the maximum achieved N-factors: reaching values of approximately 5 for $f_0 \approx 1$ kHz. In invoking the spatial evolution as depicted in Fig. 6(a), however, the *type*-III mechanism is found to reach maximum amplification at a significantly farther upstream station (at $x_{\perp}/\delta_0 = 386$ for $f_0 = 1$ kHz) than *type*-I. In particular, note that the dash-dotted lines indicate the *type*-I N-factors for $f_0 \approx 1$ kHz. This should hence provide an appropriate condition to excite the *type*-III mechanism.

In what follows, we will compare the DNS versus BiGlobal stability results. In this comparison, there are several potential sources for discrepancies:

- the present stability equations are discretized differently than the Navier-Stokes equations in the DNS.
- the BiGlobal stability equations are obtained as a simplification of the three-dimensional linearized Navier-Stokes equations. In particular, the out-of-plane variation of the base flow is neglected.
- the stability approach models linear perturbations, while the DNS permits non-linear disturbance evolution. This is expected to affect results at large $x_{\perp}$, when large amplitudes are attained.
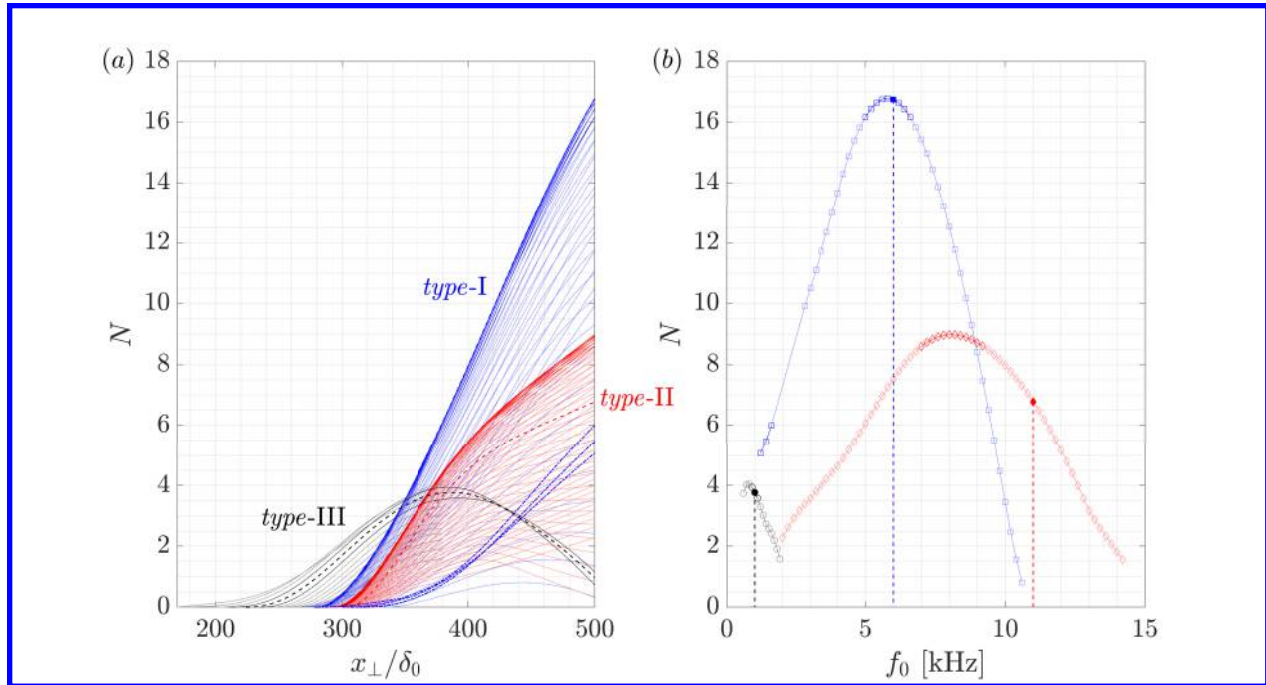
10

Figure 6 *N*-factor (*a*) curves versus $x_\perp$ and (*b*) maximum in $x_\perp$ versus f_0 (*type*-I: squares, II: diamonds, III: circles); note the horizontal correspondence between the subplots. Targeted modes and corresponding frequencies are dashed; the *type*-I *N*-factor curves for $f_0 \in [1.2; 1.6]$ kHz are dash-dotted; symbols in (*b*) indicate calculated datapoints.

- the wall-forcing approach in the DNS does not force the secondary instability mechanisms purely, or in an isolated sense, the induced perturbations are subject to a receptivity process into the shear layers supporting the instability mechanisms.
- although this is not expected to yield a noticeable difference, the stability results rely on a continuous Fourier transform in time, while a discrete transform is used for the DNS data.

B. Unsteady perturbation evolution for $f_0 = 1$ kHz

Considering monochromatic unsteady disturbances with $f_0 = 1$ kHz, as anticipated, the *type*-III mechanism manifests as the main instability in both the DNS and the BiGlobal stability results. Figure 7 illustrates the organization of the unsteady perturbation field at different $x_\perp$-locations by portraying $\sum_{j=-M_z}^{M_z} u'_{(1,j)}$. That is, the superposition of spanwise Fourier modes with associated fundamental temporal frequency $f_0 = 1$ kHz. The location and topology of this *total* unsteady disturbance field in the near-wall shear layer is in qualitative agreement with the results of previous numerical and theoretical work which identified this instability mechanism as of *type*-III (Högberg and Henningson, 1998, Bonfigli and Kloker, 2007, Janke and Balakumar, 2000). The classical literature on crossflow instabilities attributes the nature of this secondary eigenmode to the interaction between primary travelling and primary stationary crossflow disturbances; see the analysis provided by Fischer and Dallmann (1991).

Initially at $x_\perp/\delta_0 = 316$ (Fig. 7(*a*)), the secondary eigenmode topology from DNS and stability analysis are in good agreement. Whereas the main area of influence of the secondary eigenmode is common in both methods, minor discrepancies arise in the near-wall region. When moving in $x_\perp$, see Fig. 7(*b,c*), the unsteady disturbance shape expands towards the *shoulder* of the stationary crossflow vortex; as it was elaborated upon before (§ III), the development of the stationary crossflow vortex in $x_\perp$ carries growth of the shear layers embedding it. This upward expansion of the unsteady disturbance system is observed in both the DNS and the BiGlobal results. At the same time, both methods capture an increase of the perturbation strength in the lower portion of the distorted base flow for increasing $x_\perp$. When moving farther in $x_\perp$, major discrepancies between DNS and stability analysis arise in the upper portion of the crossflow vortex. The BiGlobal eigenmode shape rapidly expands in $x_\perp$ along the top of the crossflow vortex, a feature which does
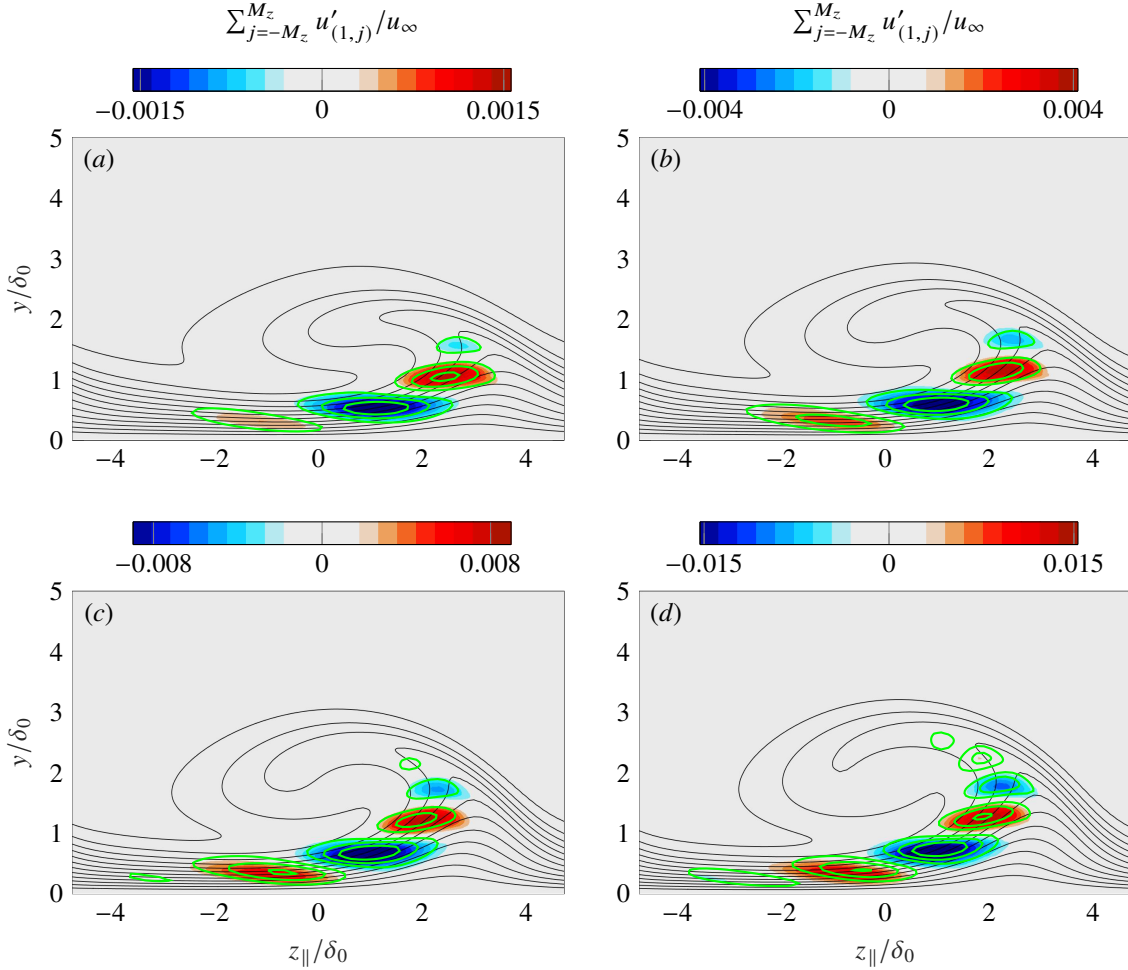
11

Figure 7   Organization of the unsteady perturbation field $\sum_{j=-M_z}^{M_z} u'_{(1,j)}$ from DNS (color map) and BiGlobal (solid green) at $x_\perp/\delta_0 = 316$ (*a*), 341 (*b*), 365 (*c*), 390 (*d*). Isolines of distorted base flow (solid black).

not manifest in the DNS results. Figure 7(*d*) depicts an $x_\perp$-station where the aforementioned effect starts to appear visually evident. The disagreement in the near-wall region becomes more pronounced as well.

To gain further insight into the secondary perturbation behaviour, we next present and discuss the topology of the individual spanwise Fourier modes composing the disturbance shape previously illustrated in Fig. 7. In particular, following Definition 5, Fig. 8 portrays the unsteady disturbance shape of $u'_{(1,j)}, |j| \leq 3$, at $x_\perp/\delta_0 = 365$. It shall be noted that in a three-dimensional boundary layer, disturbances with $\omega = k\omega_0 \neq 0$, $\beta = j\beta_0 \neq 0$ represented as a Fourier series do not hold symmetry in z. That is, whereas in a two-dimensional boundary layer $\tilde{\mathbf{v}}_{(k,-j)} = \begin{bmatrix} \tilde{u}_{(k,j)} & \tilde{v}_{(k,j)} & -\tilde{w}_{(k,j)} \end{bmatrix}^\mathrm{T}$ (Herbert, 1993), this does not hold in the present swept-wing boundary layer. The latter is highlighted by the different perturbation topology associated to $u'_{(1,\pm j)}$ in Fig. 8. Fourier modes with $\beta < 0$ represent perturbation structures propagating with the crossflow vortex in the outboard leading-edge-parallel direction, $z_\parallel < 0$, whereas those with $\beta > 0$ propagate against the crossflow vortex in the inboard leading-edge-parallel direction, $z_\parallel > 0$. Strong topological differences are observed as well between modes $u'_{(1,j)}, j = -1, -2, -3$. Overall, we find a reasonably good agreement between the results from DNS and stability analysis in terms of secondary eigenmode shape of individual Fourier modes (Fig. 8).

An agreement between methods is obtained as well when comparing the perturbation amplification factors in $x_\perp$; see Fig. 9. In the DNS, after a stage of exponential growth, the perturbation components $|\tilde{u}|_{(1,-1)}$ and $|\tilde{u}|_{(1,-2)}$ become gradually stabilised in $x_\perp$ for $x_\perp/\delta_0 > 410$, as highlighted by their positive chordwise growth rate in this region. On the
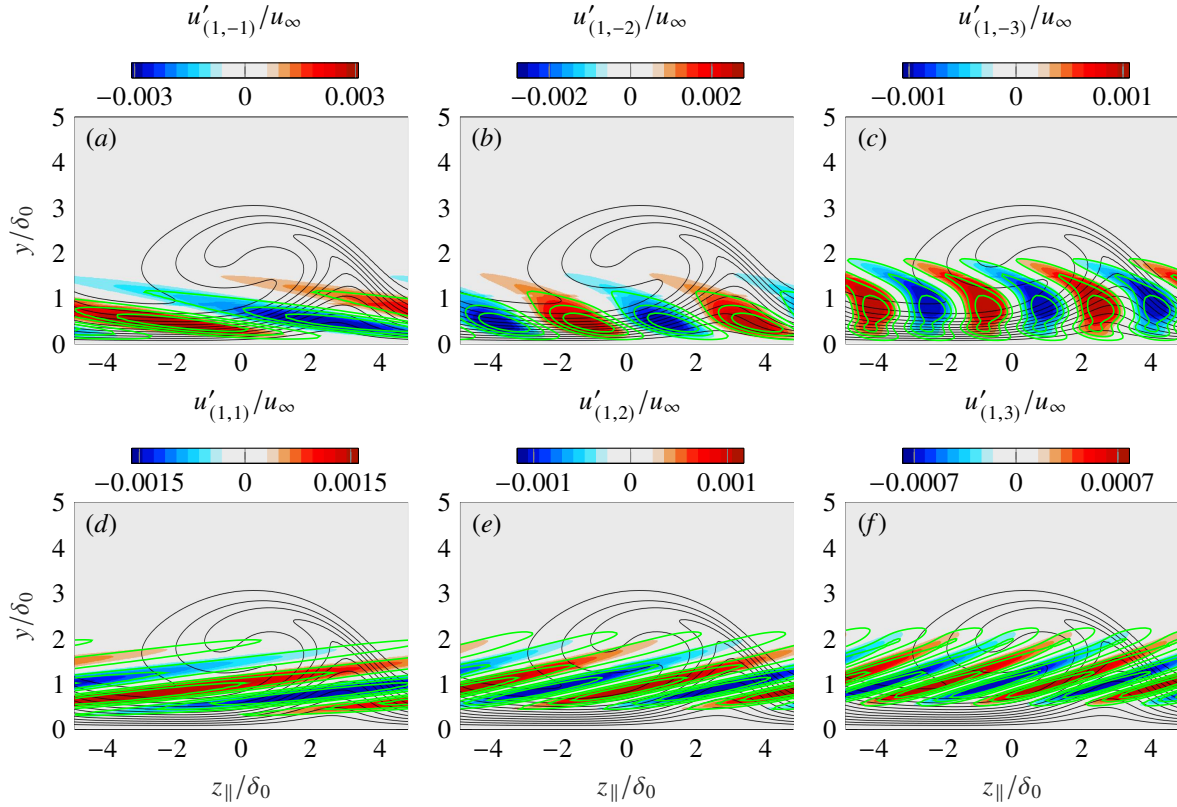
12

Figure 8 **Unsteady perturbation organization from DNS (color map) and BiGlobal (solid green) at** $x_\perp/\delta_0 = 365$**:** $u'_{(1,-1)}$ **(***a***),** $u'_{(1,-2)}$ **(***b***),** $u'_{(1,-3)}$ **(***c***),** $u'_{(1,1)}$ **(***d***),** $u'_{(1,2)}$ **(***e***),** $u'_{(1,3)}$ **(***f***). Isolines of distorted base flow (solid black).**
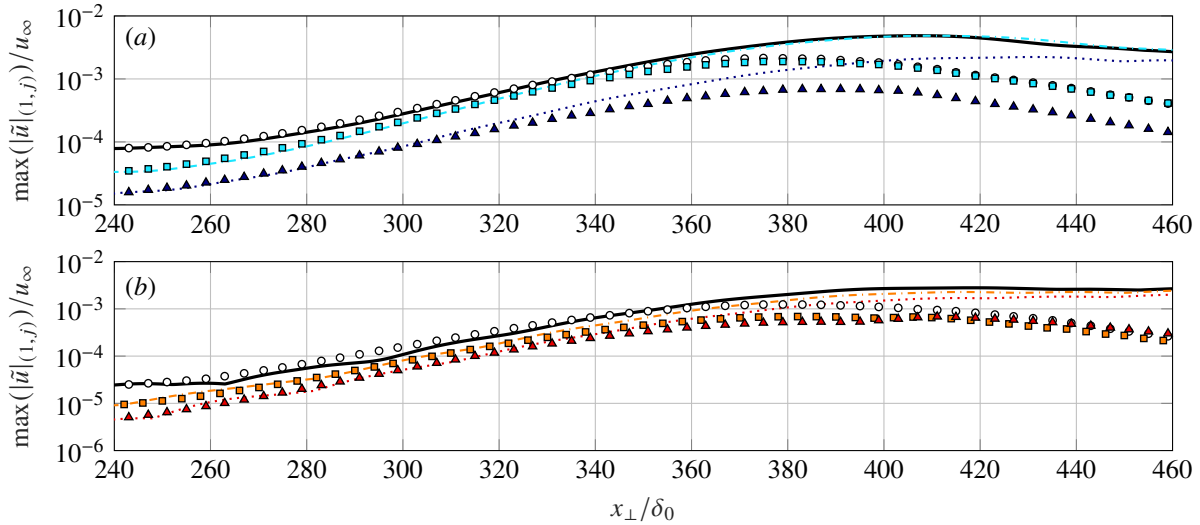

Figure 9 **Chordwise evolution of the amplitude** $|\tilde{u}|_{(1,j)}^{\max}$ **from DNS (lines) and BiGlobal (symbols):** $j = -1$ **(solid black and circles),** -2 **(dash-dotted cyan and squares),** -3 **(dotted blue and triangles) (***a***),** $j = 1$ **(solid black and circles),** 2 **(dash-dotted orange and squares),** 3 **(dotted red and triangles) (***b***).**
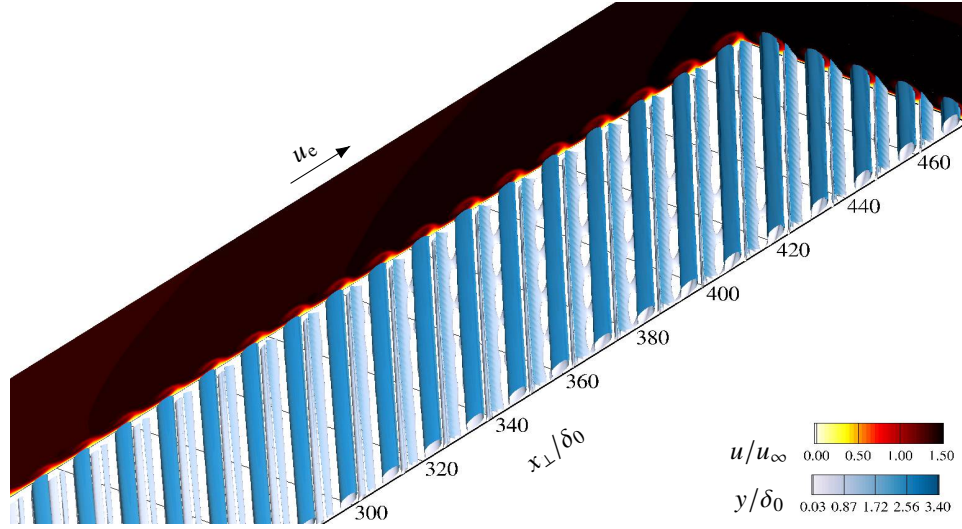
13

Figure 10   Instantaneous Q-criterion isosurface colored by wall distance and y-$z_{\|}$, $x_{\perp}$-y planes of instantaneous chordwise velocity. The DNS data are duplicated 4 times in $z_{\|}$ in a periodic manner for illustration purposes.

other hand, the component $|\tilde{u}|_{(1,-3)}$ displays a rather constant amplification in this regime. The amplification curves corresponding to the stability approach display significant stabilization in the $x_{\perp}$-range where the DNS curves exhibit mild stabilization or reach a plateau; the large differences between both methods in this regime highlights that the perturbation growth in the DNS is affected by non-linear interactions.

At the location of the wall forcing, only disturbances with $\beta = \beta_0$ are explicitly modulated; the associated harmonic spanwise components (i.e., $|\tilde{u}|_{(1,-2)}$, $|\tilde{u}|_{(1,-3)}$, etc.) are initially induced by the latter and thus first arise with a smaller amplitude than the fundamental component. This is illustrated in Fig. 9. However, sufficiently downstream of the forcing location, the secondary component $|\tilde{u}|_{(1,-2)}$ displays a growth rate larger than the fundamental component and reaches the outflow zone with a similar amplitude.

The effect of the unsteady disturbance growth on the instantaneous three-dimensional flow behaviour is illustrated in Fig. 10. In a fashion similar to the stationary developed flow field discussed in previous sections (Fig. 2), the main feature is the stationary crossflow vortices identified as isosurfaces of Q-criterion. When moving in $x_{\perp}$, a weak modulation of the near-wall Q-criterion isosurfaces in the $x_{\perp}$- and $z_{\|}$-directions is captured. This is naturally linked to the aforementioned unsteady perturbation eigenmode which lies close to the wall. The Q-criterion isosurface modulation is visually more evident at $x_{\perp}/\delta_0 \approx 400$, the chordwise location at which the perturbation amplitude attains its maximum value; see Fig. 9. Unsurprisingly, as the instability mechanism reduces its amplitude close to the outflow (Fig. 9), the modulation of the near-wall isosurface vanishes; see Fig. 10.

C. Unsteady perturbation evolution for $f_0 = 6$ kHz

Considering monochromatic disturbances with $f_0 = 6$ kHz, the BiGlobal stability approach indicates that the *type*-I instability eigenmode is the most amplified. Therefore, this mechanism is expected to dominate the perturbation dynamics in the DNS.

Figure 11 portrays the *total* perturbation shape in the DNS at different $x_{\perp}$-stations. We associate the perturbation contours localized in the outer side of the upwelling region of the stationary crossflow vortex to the *type*-I mechanism. This is substantiated in that the location of maximum perturbation strength coincides with the location of the maximum spanwise shear in the distorted base flow, $\partial u_{\mathrm{DB}}/\partial z > 0$. Furthermore, the topology of these perturbation contours qualitatively resembles that reported in previous numerical and theoretical investigations, which linked this unsteady mechanism to the *type*-I kind (Malik et al., 1999, Högberg and Henningson, 1998, Wassermann and Kloker, 2002, Bonfigli and Kloker, 2007, Janke and Balakumar, 2000). Overall, Fig. 11 and Fig. 12 show a good match of the DNS perturbation contours with the BiGlobal eigenfunctions considering the *total* perturbation shape and the individual Fourier components.

In noting that the amplification factors corresponding to the *type*-II mechanism are only about $\Delta N = -0.5$ smaller
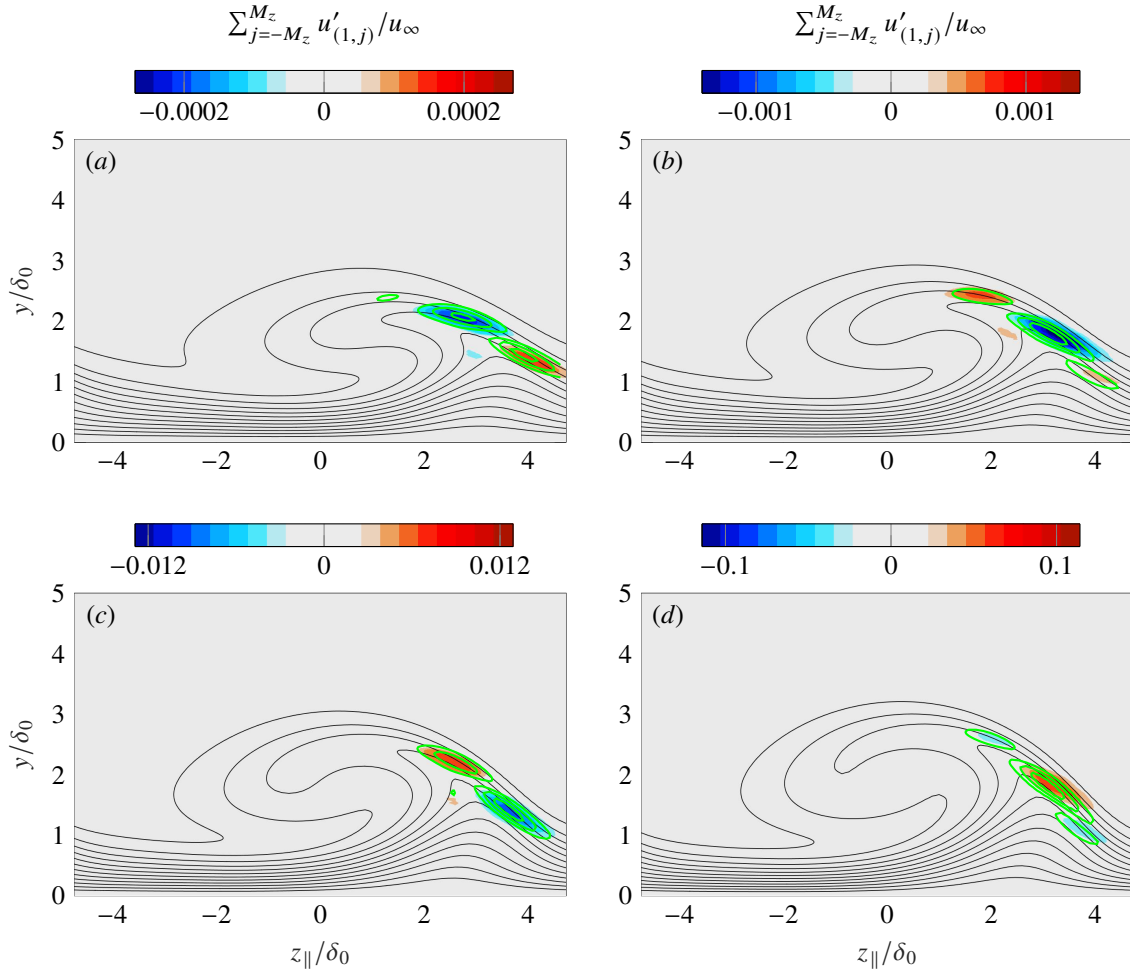
14

Figure 11 **Organization of the unsteady perturbation field** $\sum_{j=-M_z}^{M_z} u'_{(1,j)}$ **from DNS (color map) and BiGlobal (solid green) at** $x_\perp/\delta_0 = 316$ **(***a***),** 341 **(***b***),** 365 **(***c***),** 390 **(***d***). Isolines of distorted base flow (solid black).**

than those for *type*-I, the emergence of the perturbations that are highly reminiscent of the *type*-I mechanism in the DNS appears to overshadow possible *type*-II disturbances (§ IV.A). The *type*-II instability mechanism lies on the inclined shear layer on top of the crossflow vortex. Nonetheless, as it will be discussed below, there is evidence supporting the existence of the *type*-II instability mechanism in the present DNS. Wassermann and Kloker (2002) report that *type*-II disturbances are not observed in the *physically more relevant* DNS cases, but they develop in base flows distorted by a sub-critical stationary crossflow mode. This is ascribed by Wassermann and Kloker (2002) to the narrow spacing between the stationary vortices in the latter case, potentially weakening the growth of the *type*-I mechanism and thus facilitating the development of the *type*-II mechanism. However, the *type*-II kind has been reported in other numerical experiments considering critical stationary crossflow conditions; see Choudhari et al. (2013b) and Li et al. (2017), for instance.

Refocusing the attention to the most amplified mechanism, the *type*-I kind, the corresponding instability growth is quantitatively characterized in Fig. 13. Upon comparing the DNS versus the stability data, a good match is achieved while permitting an underestimation of the growth rate by the BiGlobal stability approach for $x/\delta_0 \leq 330$. The spanwise harmonics have very similar growth rates.

The amplification in $x_\perp$ of the initially *small*-amplitude perturbations leads to laminar breakdown near the end of the computational domain, as it appears evident in Fig. 14 depicting instantaneous Q-criterion isosurfaces. Therefore, the current results are representative of laminar-turbulent transition triggered by monochromatic unsteady forcing and primarily induced by the growth of the *type*-I instability mechanism. Next, we elucidate on the role of the secondary
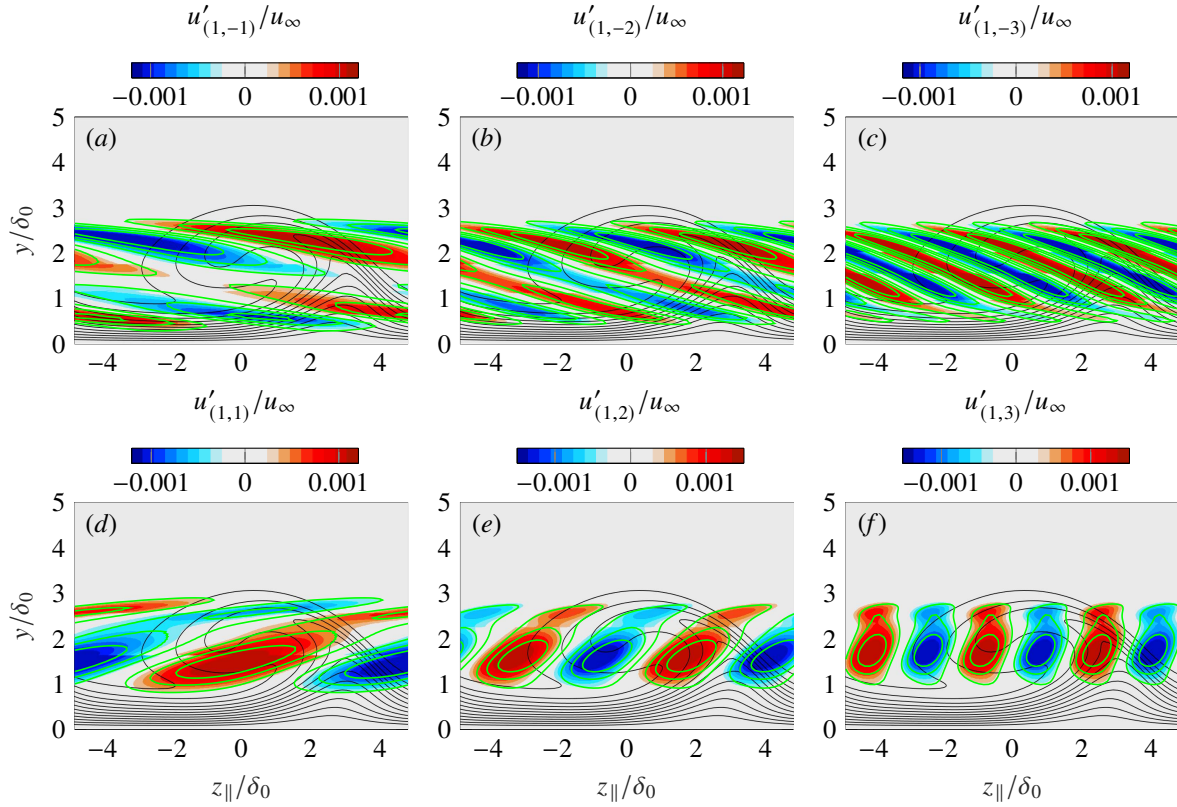
15

Figure 12   Unsteady perturbation organization from DNS (color map) and BiGlobal (solid green) at $x_\perp/\delta_0 = 365$: $u'_{(1,-1)}$ **(a),** $u'_{(1,-2)}$ **(b),** $u'_{(1,-3)}$ **(c),** $u'_{(1,1)}$ **(d),** $u'_{(1,2)}$ **(e),** $u'_{(1,3)}$ **(f). Isolines of distorted base flow (solid black).**
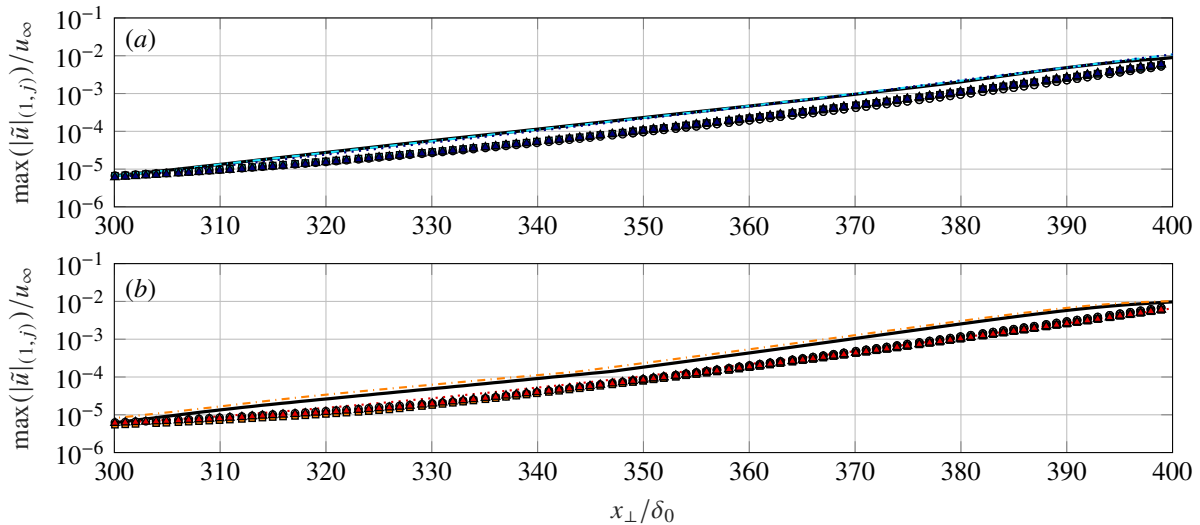

Figure 13   Chordwise evolution of the amplitude $|\tilde{u}|^{\mathbf{max}}_{(1,j)}$ from DNS (lines) and BiGlobal (symbols): $j = -1$ **(solid black and circles),** -2 **(dash-dotted cyan and squares),** -3 **(dotted blue and triangles) (a),** $j = 1$ **(solid black and circles),** 2 **(dash-dotted orange and squares),** 3 **(dotted red and triangles) (b).**
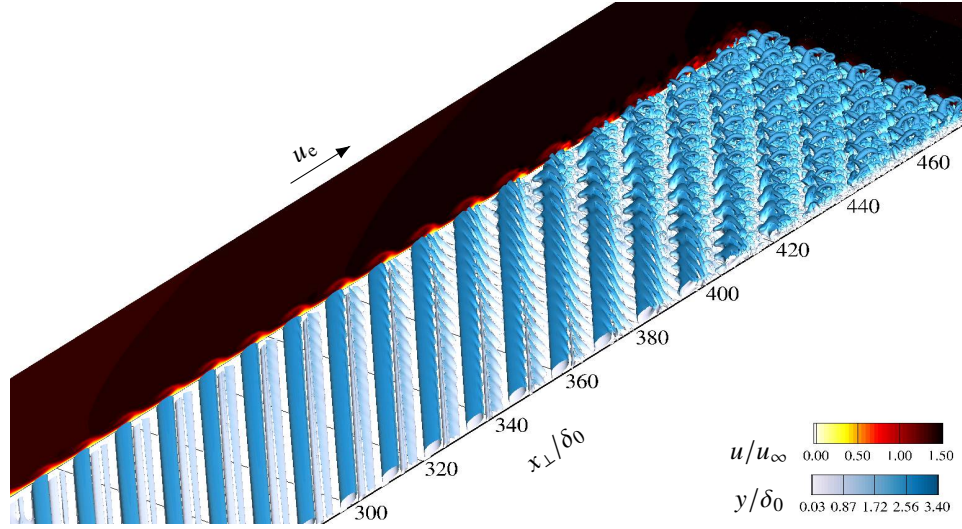
16

Figure 14   Instantaneous Q-criterion isosurfaces colored by wall distance and y-$z_{\parallel}$, $x_{\perp}$-y planes of instantaneous chordwise velocity. The DNS data are duplicated 4 times in $z_{\parallel}$ in a periodic manner for illustration purposes.
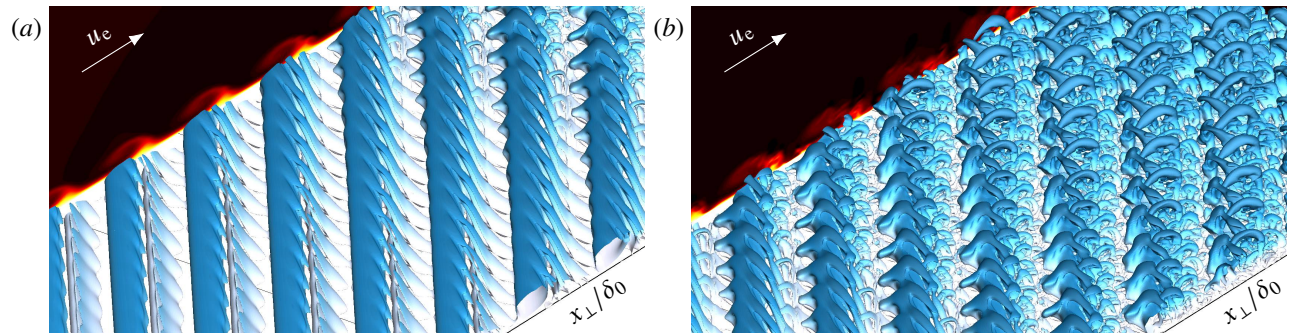

Figure 15   Zoom of instantaneous Q-criterion isosurfaces colored by wall distance and $x_{\perp}$-y plane of instantaneous chordwise velocity at $x_{\perp}/\delta_0 \approx 370$ (*a*), 410 (*b*). The DNS data are duplicated 4 times in $z_{\parallel}$ in a periodic manner for illustration purposes.

instability growth in the ultimate breakdown process. The *type*-I-dominated case as recently reported by Li et al. (2016) and Li et al. (2017) is similar to the presently considered case.

A detailed representation of the breakdown mechanisms is shown in Fig. 15, zooming near the end of the domain in Fig. 14. Gradually when moving in $x_{\perp}$, the Q-criterion isosurfaces display modulation of the region containing the lateral inclined shear layer. This phenomenon precedes the formation of large-scale ridge-like structures. The axis of these new structures is elevated with respect to the wall (i.e., with respect to the $x_{\perp}$-$z_{\parallel}$ plane) and is inclined with respect to the axis of the stationary crossflow vortices projected in the $x_{\perp}$-$z_{\parallel}$ plane. A significantly different orientation between the axis of the ridge-like structures and that of the crossflow vortices is widely reported in the literature (Wassermann and Kloker, 2002, Serpieri and Kotsonis, 2016, Bonfigli and Kloker, 2007, Janke and Balakumar, 2000). As noted by Serpieri and Kotsonis (2016), the characteristic orientation developed by the new prominent *type*-I-related structures is a consequence of the fact that they span along a large portion of the boundary layer in y; hence, their lower and upper parts are advected at different velocities.

Sufficiently upstream, the crossflow vortices coexist with the ridge-like structures while the former maintain their topological features rather invariantly. Moving farther in $x_{\perp}$, downstream of $x_{\perp} \approx 370$, the upper part of the stationary crossflow vortex becomes modulated as well, which is potentially a consequence of *type*-II amplification. This would be substantiated in that the new structures arising on the crest of the crossflow vortices, which develop a pointed arch

17

shape, qualitatively resemble the upper large-scale structures reported by Li et al. (2016, 2017), who associate these structures to the growth of the *type*-II instability. Eventually when moving in $x_\perp$, the lateral ridge-like structures become connected with the structures arising on the crest of the crossflow vortices. This could possibly point towards non-linear interaction between *type*-I and *type*-II perturbations when sufficiently large amplitudes are attained. However, whereas the interaction between the upper part of the ridge-like structures and the legs of the pointed arch-shape structures appears evident in our results, Li et al. (2017) argue that both aforementioned structures develop in distinct locations and thus do not display strong interaction.

At $x_\perp/\delta_0 = 414$, two distinct families of hairpin vortices are visually captured. They all initially move along the trajectory of the distorted crossflow vortices, but reside at different wall-normal locations. On the one hand, a first group of hairpin vortices develops close to the wall, around the lower part of the ridge-like structures. Their point of inception is $x_\perp/\delta_0 \approx 400$. On the other hand, at $x_\perp/\delta_0 \approx 412$ a second family of hairpin vortices is induced farther from the wall, around the legs of the pointed arch-shaped structures that form on top of the crossflow vortices. In the presently studied case, transition is ultimately triggered by the non-linear spreading near the wall, which appears to be linked to the action of the *type*-I mechanism and the associated near-wall hairpin vortices. Contrarily, the large-scale pointed arch-shaped structures and the second generation of hairpin vortices are maintained *far* from the wall. This suggest that, despite attaining significantly large amplitudes, they play a secondary role in the ultimate laminar-turbulent transition mechanism. This is in line with observations of Li et al. (2016, 2017).

V. Conclusions

Direct Numerical Simulations (DNS) and linear spanwise BiGlobal stability analysis are carried out to investigate the evolution of secondary instabilities in a three-dimensional swept-wing boundary layer that is preconditioned by imposing the most amplified stationary-crossflow perturbation. The analysis is carried out for single-frequency unsteady disturbances with $f_0 = 1$ kHz and $f_0 = 6$ kHz; the two cases are treated and analyzed independently. In this article, we identify and describe the behaviour of two main secondary instability mechanisms that develop on the primary crossflow-distorted state. The *type*-III eigenmode is the dominant instability in the lower frequency case ($f_0 = 1$ kHz). Considering $f_0 = 6$ kHz, the *type*-I (or z-)eigenmode and the *type*-II (or y-)eigenmode are both found to be highly unstable from the results of the stability analysis. When forcing this frequency in the DNS, the *type*-I mechanism is found to dominate the perturbation dynamics. Laminar-turbulent transition is captured in the $f_0 = 6$ kHz case; thus, the present results are representative of a stationary-crossflow breakdown scenario where the *type*-I instability leads the process. Good agreement between DNS and stability analysis in terms of perturbation organization (i.e., *shape*) around the crossflow vortices and amplification factors is obtained for all cases studied.

The stationary distorted base flow, i.e., the superposition of the unperturbed laminar base flow and the stationary crossflow instability, used as primary state for the secondary instability analysis, is characterized by co-rotating (crossflow) vortices which significantly deform the boundary layer. In the DNS, unsteady perturbation growth is triggered via wall forcing upstream of the neutral point, imposing a time-periodic modulation of the wall-normal-velocity. The unsteady perturbation behaviour is recovered from the DNS by Fourier-decomposing the instantaneous flow field in the leading-edge-parallel (or spanwise) direction and in time. The extracted spatio-temporal Fourier modes are used to compare the perturbation evolution between DNS and the BiGlobal stability approach.

In previous investigations, major discrepancies between DNS and stability methods were ascribed to the sensitivity of the latter to the representation of the distorted base flow in the stability problem (Bonfigli and Kloker, 2007). In the present work, the problem formulation considers a non-orthogonal coordinate system. Accordingly, it is made possible to simultaneously account for periodicity conditions in the leading-edge-parallel direction, $z_\parallel$, and the slow variation of the base flow along the trajectory of the crossflow vortices. This trajectory is found to be close to the inviscid-streamline direction for a large spatial extent. The satisfaction of the slow-variation condition reduces the underlying modeling error of the two-dimensional stability approach, in demand for the condition of flow invariance in one spatial direction. This solves the base-flow-extraction ambiguities pointed out by (Bonfigli and Kloker, 2007, §4.2).

Considering unsteady disturbance evolution for $f_0 = 1$ kHz, the *total* perturbation shape (i.e., the superposition of spanwise Fourier modes associated to the fundamental temporal frequency) of the associated *type*-III eigenmode is initially localized in the near-wall shear layer. As the stationary crossflow vortex develops and grows in the leading-edge-orthogonal direction, $x_\perp$, the secondary eigenmode shape gradually expands towards the inner side of the upwelling region of the crossflow vortex. For a large range in $x_\perp$ downstream of the neutral point location, good agreement in terms of perturbation organization is reported between DNS and the BiGlobal stability approach. Disagreement between methods gradually arises when moving sufficiently downstream; the BiGlobal eigenmode topology expands towards the upper part of the crossflow vortex, which is a feature that is not captured in the DNS.

A matching perturbation shape between methods is obtained as well when comparing the topology of individual Fourier modes associated to a particular combination of temporal, f, and spanwise, β, frequencies. It is noted that topological differences exist when comparing the different Fourier modes with $\beta < 0$, i.e., perturbation structures propagating in the outboard leading-edge-parallel direction, $z_\parallel < 0$. This contrasts with the rather similar shape displayed by perturbation structures with $\beta > 0$, i.e., perturbations propagating in the inboard leading-edge-parallel direction, $z_\parallel > 0$. The amplitude evolution of the spanwise Fourier modes attributed to the *type*-III eigenmode displays an excellent match between methods for a significant downstream region. The maximum amplification factor of the *total* disturbance is attained upstream of the end of the computation domain. Close to the outflow, unsteady disturbances display mild and strong stabilization in the DNS and stability approach, respectively; the large differences between methods in this regime highlights that the DNS perturbation behaviour is non-linearly dominated.

As mentioned, the perturbation dynamics are dominated by the *type*-I instability when forcing the flow field at $f_0 = 6$ kHz. Although the stability approach points out that *type*-II disturbances are highly unstable as well, they are likely overshadowed by those attributed to *type*-I. This has consequently limited a thorough comparison of *type*-II growth-rate evolution between DNS and the BiGlobal stability approach. The most amplified perturbations are found to be dominant in the shoulder of the crossflow vortex. In the literature, this type of disturbances are often attributed to the *type*-I secondary instability. Upon comparing the total perturbation shape as computed with DNS and the stability approach, an excellent match is achieved. The same applies to the shape of the spanwise Fourier modes associated to the *type*-I eigenmode. The amplitude evolution of these Fourier modes, however, is found to be slightly underestimated

19

initially by the BiGlobal stability approach.

Breakdown of the stationary crossflow vortices induced by the growth of secondary instabilities is captured within the DNS domain only for the $f_0 = 6$ kHz case. The breakdown scenario is dominated by *type*-I perturbations. The stages of the breakdown process are detailed as follows: the growth of the initially small-amplitude *type*-I disturbances modulates the shear layer at the lateral part of the crossflow vortex. This modulation precedes the formation of large-scale ridge-like structures which span over a large portion of the boundary layer in the wall-normal direction. A new family of hairpin vortices moving along the trajectory of the distorted crossflow vortices is induced in the lower part of the ridge-like structures. The hairpin structures reside close to the wall and appear to initiate the non-linear spreading in the near-wall portion of the boundary layer ultimately leading the transition process. On the other hand, the growth of structures that could potentially be related to the *type*-II disturbances on the crest of the crossflow vortex induces a second family of large-scale hairpin vortices which are maintained sufficiently far from the wall and thus appear to play a less critical role in triggering laminar-turbulent transition.

VI. Appendix

A. Non-orthogonal coordinate system

The perturbation problem is periodic in the direction parallel to the leading edge, $z_{||}$, while the distortion of the crossflow vortices causes the variation of the base flow to be least in the direction of the crossflow vortices' axes. The latter direction differs from the leading-edge-orthogonal direction, $x_\perp$, by an amount approximately equal to the sweep angle. This implies that the stability problem ought to be formulated in a non-orthogonal coordinate system in order to minimize the model error.

Using a non-orthogonal coordinate system is uncommon, hence we briefly elaborate on the formulation of the governing equations in this appendix. See Fig. 16 and Eqs. (11) for the relation between the various coordinates that are used. In what follows, the variation of the angle θ with $x_\perp$ will be assumed to be negligible; Fig. 4 supports that $d\theta/dx_\perp$ is small for the streamwise stations considered for the stability analysis, i.e., $x_\perp/\delta_0 > 170$. The angle θ is drawn as positive in Fig. 16. Note that, due to the use of a negative sweep angle in the present study, θ will be negative as well. To re-express the equations, the first step is to realize that the same function is expressed in different ways:

$$f_\perp(x_\perp, z_{||}) = f(x, z). \tag{10}$$

$$
\begin{aligned}
x &\overset{(a)}{=} x_\perp/\cos\theta = x_\perp \sec\theta \\
z &\overset{(b)}{=} z_{||} - x_\perp \tan\theta \\
x_\perp &\overset{(c)}{=} x \cos\theta \\
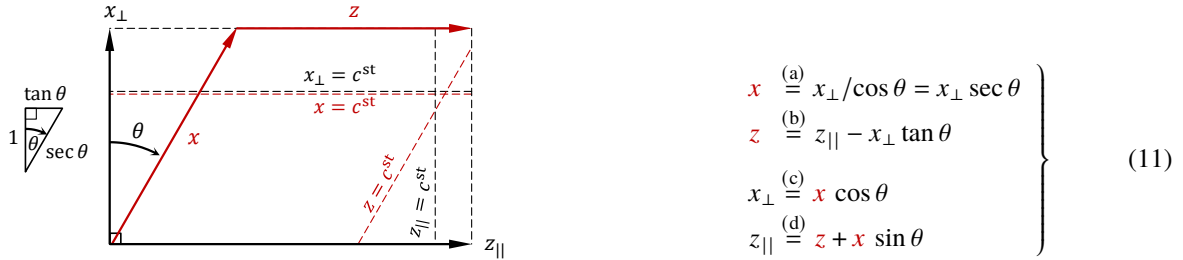z_{||} &\overset{(d)}{=} z + x \sin\theta
\end{aligned}
\tag{11}
$$

Figure 16   Coordinate systems and transformations.

However, the expression for the function changes upon changing the coordinate system. Hence $f_\perp(x, z) \neq f(x, z)$ and $f(x, z_{||}) \neq f(x, z)$, for example; but $f(x, z) = f(x_\perp \sec\theta, z_{||} - x_\perp \tan\theta)$. The original equations are given in terms of the orthogonal $x_\perp$- and $z_{||}$-coordinates. Therefore we want to rewrite the derivatives with respect to those coordinates, which is done as follows:

$$\left.\frac{\partial f_\perp}{\partial x_\perp}\right|_{z_{||}} = \left.\frac{\partial f}{\partial x_\perp}\right|_{z_{||}} = \left.\frac{\partial f}{\partial x}\right|_z \left.\frac{\partial x}{\partial x_\perp}\right|_{z_{||}} + \left.\frac{\partial f}{\partial z}\right|_x \left.\frac{\partial z}{\partial x_\perp}\right|_{z_{||}} = \left.\frac{\partial f}{\partial x}\right|_z \sec\theta - \left.\frac{\partial f}{\partial z}\right|_x \tan\theta; \tag{12a}$$

$$\left.\frac{\partial f_\perp}{\partial z_{||}}\right|_{x_\perp} = \left.\frac{\partial f}{\partial z_{||}}\right|_{x_\perp} = \left.\frac{\partial f}{\partial x}\right|_z \left.\frac{\partial x}{\partial z_{||}}\right|_{x_\perp} + \left.\frac{\partial f}{\partial z}\right|_x \left.\frac{\partial z}{\partial z_{||}}\right|_{x_\perp} = 0 + \left.\frac{\partial f}{\partial z}\right|_x, \tag{12b}$$

where Eq. (10) is used in the equation on the far left and Eqs. 11 to evaluate the partial derivatives in letting $f = f(x(x_\perp), z(x_\perp, z_{||}))$. The higher-order and inverse relations are obtained similarly, see Groot and Eppink (2021) for further details and the resulting system of equations.

Acknowledgments

References

Henke, R., ""A 320 HLF fin" flight tests completed," *Air Space & Europe*, Vol. 1, No. 2, 1999.

Malik, M. R., Crouch, J. D., Saric, W. S., Lin, J. C., and Whalen, E. A., "Application of drag reduction techniques to transport aircraft," *Encyclopedia of Aerospace Eng.*, 2015, pp. 1–10.

Rius-Vidales, A. F., and Kotsonis, M., "Impact of a forward-facing step on the development of crossflow instability," *J. Fluid Mech.*, Vol. 924, 2021, p. A34.

Mack, L. M., "Boundary-Layer Linear Stability Theory," *Special Course on Stability and Transition of Laminar Flow, AGARD 709*, AGARD, 1984.

Saric, W. S., Reed, H. L., and White, E. B., "Stability and transition of three-dimensional boundary layer," *Annu. Rev. Fluid Mech.*, Vol. 35, 2003, pp. 413–40.

Deyhle, H., and Bippes, H., "Disturbance growth in an unstable three-dimensional boundary layer and its dependence on environmental conditions," *J. Fluid Mech.*, Vol. 316, 1996, pp. 73–113.

Bippes, H., "Basic experiments on transition in the three-dimensional boundary layers dominated by crossflow instability," *Prog. Aerosp. Sci.*, Vol. 35, 1999, pp. 363–412.

Reed, H. L., Saric, W. S., and Arnal, D., "Linear Stability Theory Applied to Boundary Layers," *Annual Review of Fluid Mechanics*, Vol. 28, No. 1, 1996, pp. 389–428.

Theofilis, V., "Advances in Global Linear Instability Analysis of Nonparallel and Three-Dimensional Flows," *Progress in Aerospace Sciences*, Vol. 39, No. 4, 2003, pp. 249–315.

Van Ingen, J. L., "A suggested semi-empirical method for the calculation of the boundary layer transition region," Vth-74, Delft University of Technology, The Netherlands, 1956.

Smith, A., and Gamberoni, N., "Transition, pressure gradient and stability theory," *Aircraft Co., Report No. ES 26 388, El Segundo, CA*, 1956.

Müller, B., "Experimentelle Untersuchung der Querströmungsinstabilität im linearen und nichtlinearen Bereich des Transitiongebietes," DLR-FB 90-09, 1990.

Kachanov, Y., and Tararykin, O., "The experimental investigation of stability and receptivity on a swept wing flow," IUTAM Symp. "Laminar Turbulent Transition", 1990.

Bippes, H., *Experiments on transition in three-dimensional accelerated boundary layer flows*, Proc. R.A.S. Boundary Layer Transition and Control, Cambridge, 1991.

Bertolotti, F. P., "On the birth and evolution of disturbances in three-dimensional boundary layers," *Nonlinear Instability and Transition in Three-Dimensional Boundary Layers (ed. P. W.Duck & P. Hall)*, 1996, pp. 115–132.

Haynes, T. S., and Reed, H. L., "Simulation of swept-wing vortices using nonlinear parabolized stability equations," *J. Fluid Mech.*, Vol. 405, 2000, pp. 325–349.

Poll, D. I. A., "Some observations of the transition process on the windward face of a long yawed cylinder," *J. Fluid Mech.*, Vol. 150, 1985, pp. 329–356.

Kohama, Y., Saric, W. S., and Hoos, J. A., "A high frequency secondary instability of crossflow vortices that leads to transition," Proc. R. Aeronaut. Soc. Conf on Boundary Layer Transition & Control, 1991.

Malik, M. R., Li, F., and Chang, C.-L., "Crossflow disturbances in three-dimensional boundary layers: nonlinear development, wave interaction and secondary instability," *J. Fluid Mech.*, Vol. 268, 1994, pp. 1–36.

Malik, M. R., Li, F., Choudhari, M. M., and Chang, C.-L., "Secondary instability of crossflow vortices and swept-wing boundary-layer transition," *J. Fluid Mech.*, Vol. 399, 1999, pp. 85–115.

Fischer, T. M., and Dallmann, U., "Primary and secondary stability analysis of a three-dimensional boundary-layer flow," *Phys. Fluids A: Fluid Dynamics*, Vol. 3, No. 10, 1991, pp. 2378–2391.

Koch, W., Bertolloti, F. P., Stolte, A., and Hein, S., "Nonlinear equilibrium solutions in a three-dimensional boundary layer and their secondary instability," *J. Fluid Mech.*, Vol. 406, 2000, pp. 131–174.

Högberg, M., and Henningson, D., "Secondary instability of cross-flow vortices in falkner-skan-cooke boundary layers," *J. Fluid Mech.*, Vol. 368, 1998, pp. 339–357.

Wassermann, P., and Kloker, M., "Mechanisms and passive control of crossflow-vortex-induced transition in a three-dimensional boundary layer," *J. Fluid Mech.*, Vol. 456, 2002, pp. 49–84.

Li, F., Choudhari, M. M., and Duan, L., "Stationary crossflow breakdown due to mixed mode spectra of secondary instabilities," *AIAA Paper 2016-3789*, 2016.

Li, F., Choudhari, M. M., and Duan, L., "Stationary crossflow Breakdown due to interaction between secondary instabilities," *AIAA Paper 2017-4302*, 2017.

Serpieri, J., and Kotsonis, M., "Three-dimensional organisation of primary and secondary crossflow instability," *J. Fluid Mech.*, Vol. 799, 2016, pp. 200–245.

Bonfigli, G., and Kloker, M., "Secondary instability of crossflow vortices: validation of the stability theory by direct numerical simulation," *J. Fluid Mech.*, Vol. 583, 2007, pp. 229–272.

White, E. B., and Saric, W. S., "Secondary instability of crossflow vortices," *J. Fluid Mech.*, Vol. 525, 2005, pp. 275–308.

Groot, K., Serpieri, J., Pinna, F., and Kotsonis, M., "Secondary crossflow instability through global analysis of measured base flows," *J. Fluid Mech.*, Vol. 846, 2018, pp. 605–653.

Li, F., and Choudhari, M. M., "Spatially developing secondary instabilities in compressible swept airfoil boundary layers," *Theor. Comput. Fluid Dyn.*, Vol. 25, 2011, pp. 65–84.

Hickel, S., and Adams, N. A., "Implicit LES applied to zero-pressure-gradient and adverse-pressure-gradient boundary-layer turbulence," *Int. J. Heat Fluid Fl.*, Vol. 29, 2008, pp. 626–639.

Hickel, S., Egerer, C. P., and Larsson, J., "Subgrid-scale modeling for implicit large eddy simulation of compressible flows and shock-turbulence interaction," *Phys. Fluids*, Vol. 26, 2014, pp. 106–101.

Casacuberta, J., Groot, K. J., Ye, Q., and Hickel, S., "Transitional flow dynamics behind a micro-ramp," *Flow Turbul. Combust.*, Vol. 104, 2020, pp. 533–552.

Casacuberta, J., Hickel, S., and Kotsonis, M., "Mechanisms of interaction between stationary crossflow instabilities and forward-facing steps," *AIAA Paper 2021-0854*, 2021.

Westerbeek, S., "Development of a Nonlinear Parabolized Stability Equations (NPSE) Analysis Tool for Spanwise Invariant Boundary Layers," Master's thesis, TU Delft, 2020.

Akervik, E., Brandt, L., Henningson, D. S., Hoepffner, J., Marxen, O., and Schlatter, P., "Steady solutions of the Navier-Stokes equations by selective frequency damping," *Phys. Fluids*, Vol. 18, 2006, p. 068102.

Casacuberta, J., Groot, K. J., Tol, H. J., and Hickel, S., "Effectivity and efficiency of selective frequency damping for the computation of unstable steady-state solutions," *J. Comput. Phys.*, Vol. 375, 2018, pp. 481–497.

Hunt, J., Wray, A., and Moin, P., "Eddies, streams, and convergence zones in turbulent flows," Report CTR-S88, center for turbulence research, 1988.

Groot, K. J., and Eppink, J. L., "Stability Analysis of the Flow over a Swept Forward-Facing Step using PIV Base Flows in a Nonorthogonal Coordinate System," *AIAA paper, 2021-2908*, 2021.

Pinna, F., "Numerical study of stability of flows from low to high Mach number," Ph.D. thesis, Università di Roma - "La Sapienza", Von Kármán Institute, Rhode-Saint-Genèse, 2012.

Choudhari, M. M., Li, F., Chang, C.-L., Carpenter, M., Streett, C., Malik, M. R., and Duan, L., "Towards bridging the gaps in holistic transition prediction via numerical simulations," *21st AIAA Computational Fluid Dynamics Conference*, 2013a, p. 2718.

Li, F., Choudhari, M. M., Duan, L., and Chang, C.-L., "Nonlinear development and secondary instability of traveling crossflow vortices," *Physics of Fluids*, Vol. 26, No. 6, 2014, p. 064104.

Janke, E., and Balakumar, P., "On the secondary instability of three-dimensional boundary layers," *Theor. Comput. Fluid Dyn.*, Vol. 14, 2000, pp. 167–194.

Herbert, T., *Parabolized stability equations*, AGARD R-793, 1993.

Choudhari, M. M., Li, F., Duan, L., Chang, C.-L., Carpenter, M. H., Streett, C. L., and Malik, M. R., "Towards Bridging the Gaps in Holistic Transition Prediction via Numerical Simulations," *AIAA Paper 2013-2718*, 2013b.